nature climate change

ARTICLES

https://doi.org/10.1038/s41558-020-00943-1

Opposite response of strong and moderate positive Indian Ocean Dipole to global warming

Wenju Cai[1,2]✉, Kai Yang[3], Lixin Wu[1]✉, Gang Huang[3,4], Agus Santoso[2,5], Benjamin Ng[2], Guojian Wang[1,2] and Toshio Yamagata[6]

A strong positive Indian Ocean Dipole (pIOD) induces weather extremes such as the 2019 Australian bushfires and African floods. The impact is influenced by sea surface temperature (SST), yet models disagree on how pIOD SST may respond to greenhouse warming. Here we find increased SST variability of strong pIOD events, with strong equatorial eastern Indian Ocean cool anomalies, but decreased variability of moderate pIOD events, dominated by western warm anomalies. This opposite response is detected in the Coupled Model Inter-comparison Project (CMIP5 and CMIP6) climate models that simulate the two pIOD regimes. Under greenhouse warming, the lower troposphere warms faster than the surface, limiting Ekman pumping that drives the moderate pIOD warm anomalies; however, faster surface warming in the equatorial western region favours atmospheric convection in the west, strengthening equatorial nonlinear advection that forces the strong pIOD cool anomalies. Climate extremes seen in 2019 are therefore likely to occur more frequently under greenhouse warming.

A positive Indian Ocean Dipole (pIOD) refers to a sea surface temperature (SST) pattern that features warm anomalies in the equatorial western Indian Ocean and cold anomalies in the east, described by a positive dipole mode index (DMI)[1]. A pIOD event usually peaks in austral spring (September, October, November; SON) but starts to develop in austral winter, with an initial cooling off Sumatra–Java suppressing the local atmospheric convection there and generating anomalous southeasterly winds. The anomalous winds promote upwelling and lift the thermocline that in turn reinforces the initial cooling[1,2], a process referred to as local Bjerknes feedback. During a strong pIOD, the growth of cool anomalies causes a northwestward shift of atmospheric convection and a westward extension of the southeasterly trades that usually flow over the southern tropical Indian Ocean in austral winter and spring. The anomalous easterlies extend across the equatorial Indian Ocean, where weak westerlies normally prevail[3] (Extended Data Fig. 1). The anomalous easterly winds promote warm SST anomalies, convergence, and rainfall in the equatorial western Indian Ocean[1–3].

The altered ocean–atmosphere circulations induce weather extremes in Indian Ocean-rim countries[1–9], such as droughts, heatwaves and bushfires in Indonesia and Australia[4–7], floods and malaria outbreaks in East Africa[9,10], and coral reef death across western Sumatra[11]. During the 1997 strong pIOD event[2] (Extended Data Fig. 1), floods in the African countries led to several thousand deaths and hundreds of thousands of people displaced, whereas wildfires in the eastern Indian Ocean regions affected the lives of tens of millions[3] and the global carbon budget[12]. Similar severe impacts also occurred during the 2019 strong pIOD event[13], and Australia experienced a devastating bushfire season, referred to as the Black Summer, with a burnt area of more than 170,000 km^2, 30 people killed and 3,000 buildings destroyed[14].

Determining how pIOD SST may change under greenhouse warming is one of the most important issues in climate science; however, for several climate model generations, there has been either a lack of intermodel consensus or no statistically significant change using the conventional DMI (refs. [15–17]).

Long-standing uncertainty in projected pIOD SST change

Uncertainty in projected pIOD SST change is despite a strong intermodel consensus on a mean state change in the tropical Indian Ocean, which features equatorial easterly wind trends and a faster warming rate in the northwest than in the southeast of the tropical Indian Ocean, a shallowing equatorial thermocline[15–19], and some changes in characteristics of strong pIOD[20,21]. First, the faster warming in the west equatorial Indian Ocean facilitates an increased frequency of a westward-shifted atmospheric convergence zone from the east and hence there are more events with extreme impacts, even if SST variability does not change[20]. Second, the enhanced north-minus-south SST gradient inhibits the seasonal southward shift of the tropical Indian Ocean Intertropical Convergence Zone[21], leading to an anomalously weak convergence in the eastern Indian Ocean, particularly during a strong pIOD (Extended Data Figs. 1 and 2d–f). Third, although a projected thermocline shallowing in the eastern Indian Ocean increases the role of the relatively cold subsurface water through an increased thermocline response to winds, this is offset by a weakened response of equatorial winds to SST anomalies. The weaker wind response occurs because the lower atmosphere becomes more stable, as the low troposphere warms faster than the surface under greenhouse warming[16].

Palaeoclimate proxies show that pIOD was more intense during the past warmer period of the middle Holocene than in the twentieth century[7], and there is already an increase in the frequency and strength of pIOD events during the second half of

[1]Key Laboratory of Physical Oceanography–Institute for Advanced Ocean Studies, Ocean University of China and Qingdao National Laboratory for Marine Science and Technology, Qingdao, China. [2]Center for Southern Hemisphere Oceans Research (CSHOR), CSIRO Oceans and Atmosphere, Hobart, Tasmania, Australia. [3]State Key Laboratory of Numerical Modeling for Atmospheric Sciences and Geophysical Fluid Dynamics, Institute of Atmospheric Physics, Chinese Academy of Sciences, Beijing, China. [4]Laboratory for Regional Oceanography and Numerical Modeling, Qingdao National Laboratory for Marine Science and Technology, Qingdao, China. [5]Australian Research Council (ARC) Centre of Excellence for Climate Extremes, The University of New South Wales, Sydney, New South Wales, Australia. [6]Application Laboratory, JAMSTEC, Yokohama, Japan. ✉e-mail: wenju.cai@csiro.au; lxwu@ouc.edu.cn

the twentieth century[8]; however, climate model projections of the response of pIOD SST variability to greenhouse warming remain uncertain[15]. Using the DMI determined from the observed poles assumes that the pIOD possesses little pattern diversity and that the simulated location of pIOD SST anomaly centres across models is the same as the observed. Here we show that there are two pIOD regimes—thus requiring at least two separate indices—and that their associated anomaly patterns differ vastly from one model to another. Furthermore, there is a robust pIOD SST change if we focus on SST variability patterns and centres unique to each individual model.

Dynamics of the two distinct pIOD regimes in observations

Previous studies have shown that pIOD events display different flavours[20,22–25]. During a strong pIOD, the anomalous cooling off Java–Sumatra expands northward and then westward along the equator[20], inhibiting the seasonal southward shift of the intertropical convergence zone towards the equatorial eastern Indian Ocean and inducing a westward shift of the equatorial eastern Indian Ocean convergence zone[21], generating strong easterlies along the equator (Extended Data Fig. 1d–f). These winds in turn enhance the equatorial west-minus-east SST gradient through a positive nonlinear zonal and vertical feedback, dramatically increasing the anomalous cooling in the equatorial eastern Indian Ocean[20].

During moderate pIOD events such as in 1982, Bjerknes feedback drives moderate cooling off Sumatra–Java (Extended Data Fig. 2a–c); to the west, the dominant forcing of the broad area of warming includes an anomalous Ekman pumping that arises from westward propagation of off-equatorial downwelling Rossby waves that are generated by equatorial anomalous easterlies in the eastern Indian Ocean during the development phase, and their subsequent reflection at the western boundary as downwelling Kelvin waves[26]. Heat budget analysis shows that Ekman pumping is the dominant forcing of the warm anomalies (Extended Data Fig. 3, see also the 'Heat budget analysis' section in the Methods).

Depiction of the two distinct pIOD regimes

The large difference in the spatial pattern and the dynamics between the strong and moderate pIOD indicates that at least two indices are needed to distinguish them[13,20,27]. To construct the indices, we use the first two principal modes of an empirical orthogonal function (EOF) analysis of SON-averaged SST anomalies that cover the 1982–2015 period, each described by a principal spatial pattern and a principal component (PC) time-series that is scaled to have a variance of unity (see the 'Data, models and EOF analysis' section in the Methods). At their positive phase, EOF1 shows a cold-anomaly centre off Sumatra–Java, which is accompanied by warming in much of the tropical Indian Ocean basin, analogous to that associated with the DMI (correlation of 0.90); this is accompanied by a shoaled equatorial thermocline in the east but a deepened equatorial thermocline to the west (Fig. 1a). EOF2 exhibits a cold-anomaly maximum in the eastern equatorial region, which tends to be equatorially symmetric and extends westward (Fig. 1b). This reflects the impact of equatorial nonlinear advection[13,20,27].

The two PC time-series display a nonlinear relationship (Fig. 1c). A pIOD event can be constructed by a combination of the two EOFs to realize event diversity. Strong pIOD events appear in the quadrant in which both PCs are positive, that is, with the equatorially symmetric cold anomalies of EOF2 superimposed onto the cold anomalies off Sumatra–Java of EOF1 such that these events are dominated by cold anomalies, as occured in 1997 and 2019 (refs. [20,27]). Strong pIOD events can therefore be described by a strong pIOD index, defined as $S=(\mathrm{PC1}+\mathrm{PC2})/\sqrt{2}$. By contrast, moderate pIOD events appear in the quadrant in which PC1 is positive but PC2 is negative, such that cold anomalies in the east are weak and warm anomalies to the west dominate, as occured in 1982. Moderate pIOD events can thus be described as $M=(\mathrm{PC1}-\mathrm{PC2})/\sqrt{2}$. The two indices separate the observed pIOD events identified by the DMI into two groups: strong events such as 1994, 1997, 2006 and 2019 in the S-index (red curve); and moderate events such as the prominent 1982, 1987 and 2015 events in the M-index (green curve) (Fig. 1c,d). Our approach is similar to a previous analysis on rainfall[20], but we instead use SST, which allows depiction of both strong and moderate pIOD events using SST anomalies. This is the simplest objective description of pIOD diversity compared with other attempts[22,24].

Sea surface temperature anomaly patterns for the two types of pIOD constructed using PC1 and PC2 reproduce the salient features in raw data (Extended Data Figs. 1 and 2), in terms of dominance of the strong cold anomalies in strong pIOD events and by broad-scaled warm anomalies in moderate pIOD events, respectively (Fig. 1e,f). Dynamics that govern the ability to generate the two patterns in part depend on whether the cold anomalies grow northwest towards—and then westward along—the equator, triggering the equatorial nonlinear advective feedbacks that lead to the enhanced cooling represented by PC2, that is, PC2 is a nonlinear function of PC1, which is expressed as $\mathrm{PC2}(t)=\alpha[\mathrm{PC1}(t)]^2+\beta\mathrm{PC1}(t)+\gamma$, similar to that used for describing ENSO diversity[28,29], in which α, β and γ are the nonlinear coefficient, linear coefficient and constant of the quadratic function, respectively. For the observed, obtained from multireanalysis products (see Methods section 'Nonlinear dynamics and model selection'), the mean value of α is 0.42 (Fig. 1c). A large value of α represents strong nonlinearity that distinguishes moderate and strong pIOD events.

Simulation of the two pIOD regimes in climate models

We analyse outputs from 35 available CMIP5 (ref. [30]) and 19 CMIP6 (ref. [31]) models by applying the same EOF analysis on SON-averaged SST anomalies from the mean of the first 100 years, quadratically detrended over the full 1900–2099 period (see the 'Data, models and EOF analysis' section in the Methods). These models were forced with historical anthropogenic and natural forcings up to 2005 for CMIP5 or 2014 for CMIP6, and thereafter under a future greenhouse gas emission scenario of representative concentration pathway 8.5 (RCP8.5) for CMIP5 and the equivalent updated

Fig. 1 | Identification of observed strong and moderate pIOD events. a, SON SST and tropical vertical potential temperature anomalies (°C, colour) and wind stress anomalies (N m^{-2}, vectors) regressed onto the first principal component (PC1) of EOF of SON SST anomalies over the tropical Indian Ocean (5° S to 5° N and 40° E to 100° E) for the 1982–2015 period average across four reanalysis products (see the 'Data, models and EOF analysis' section in the Methods). Subsurface potential temperature and wind stress data are from ORA-S5. The vertical temperature anomalies are calculated as the average over 2.5° S to 2.5° N. **b**, Same as **a**, but for PC2. **c**, The nonlinear relationship between the normalized PC1 and PC2. Red dots indicate strong pIOD years (PC1 > 1 s.d. and PC2 > 0.5 s.d.); green dots denote moderate pIOD years (PC1 > 1 s.d. and PC2 < 0.5 s.d.); the black dot marks the 2019 pIOD, obtained by regressing the SST anomaly pattern over the tropical Indian Ocean in 2019 from the GODAS dataset onto the EOF1 and EOF2 patterns; and the purple curve shows a nonlinear fit $\mathrm{PC2}(t)=\alpha[\mathrm{PC1}(t)]^2+\beta\mathrm{PC1}(t)+\gamma$. **d**, The time-series of a DMI (upper panel) can be split into (red) strong ($S=(\mathrm{PC1}+\mathrm{PC2})/\sqrt{2}$) and (green) moderate pIOD ($M=(\mathrm{PC1}-\mathrm{PC2})/\sqrt{2}$) indices (lower panel) to capture the strong and moderate pIOD events in Fig. 1c. The black dashed line in upper half shows 0.75 s.d. of the DMI, whereas the red and green dashed lines in the lower half show 1.5 s.d. and 1.25 s.d. of the S- and M-index, respectively. **e**, Reconstruction of temperature anomalies (°C, colour shading) and wind stress anomalies (N m^{-2}, vectors) of strong pIOD using the two EOFs. The green boxes indicate areas used for calculating the DMI. **f**, Same as **e**, but for moderate pIOD.

scenario for CMIP6, that is, shared socioeconomic pathway 5–8.5 (SSP5–8.5) (refs. [30,31]). The simulated anomaly pattern of either the S- or M-index differs vastly from one model to another (Fig. 2a,b). In contrast to the use of the DMI, our approach accounts for diversity in patterns and thus facilitates assessment of the response of the pIOD SST variability as simulated by each individual model.

Most models examined here simulate a value of α that is lower than the observed and a total of 20 models produce a value of α that is greater than 50% of the observed (Fig. 2c). These 20 models simulate a reasonable nonlinear PC1 and PC2 relationship and the contrast in the cold- and warm-anomaly dominance between the strong and moderate pIOD events (Extended Data Fig. 4 for samples).

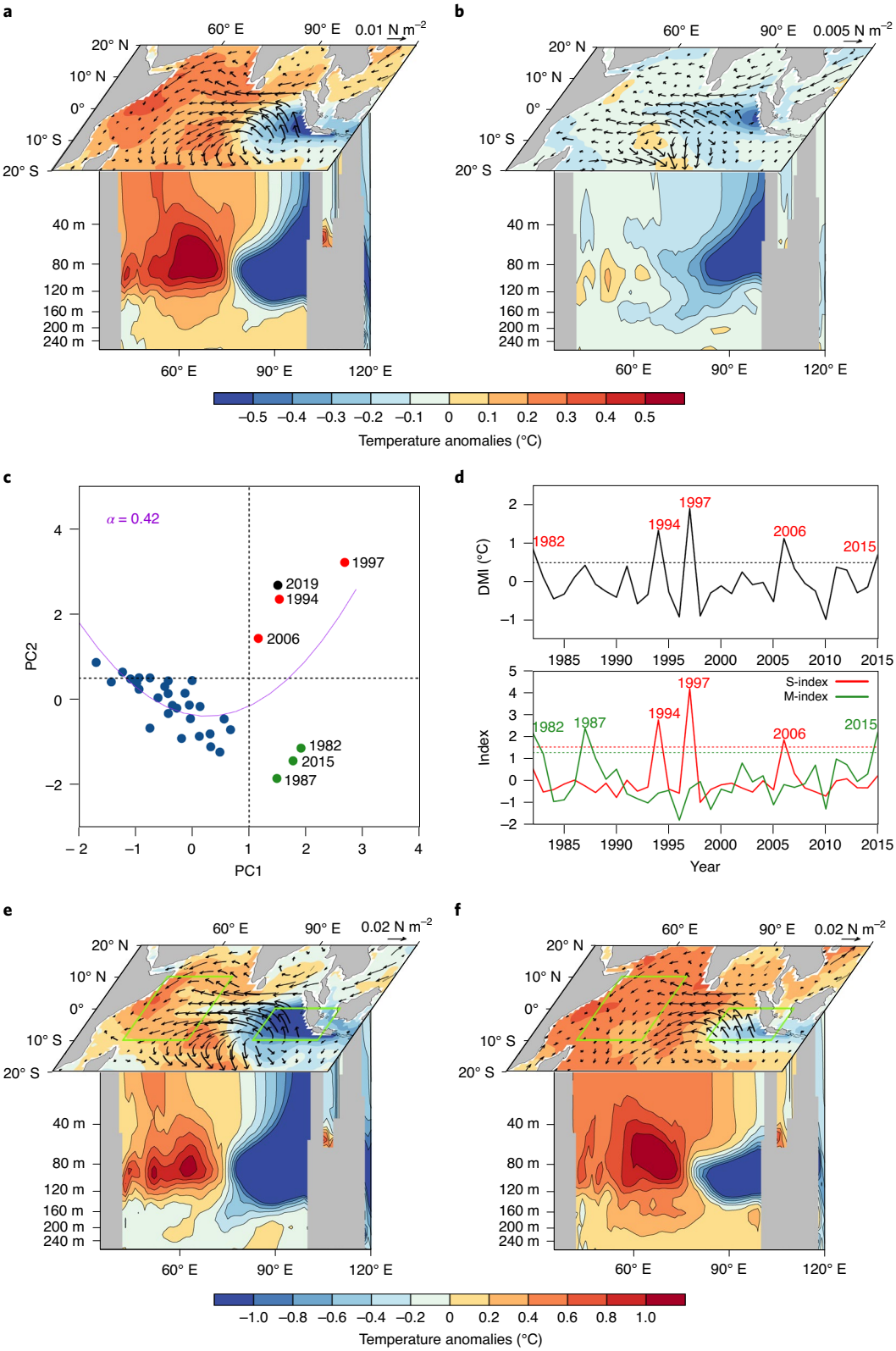

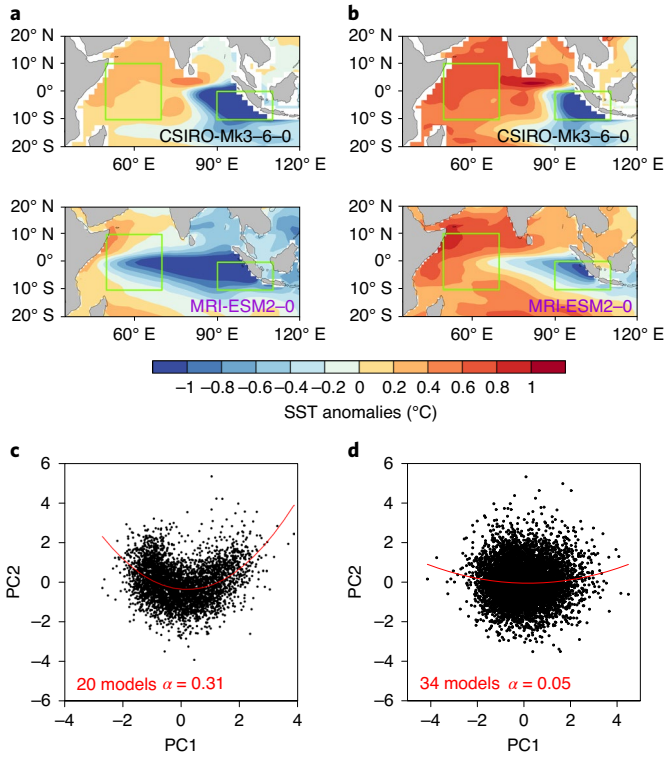

Fig. 2 | Selection of models based on pIOD nonlinearity. a, A composite of SST anomalies (in °C) for strong pIOD events (defined as S-index > 1.5 s.d.) in two models, showing vastly different pIOD patterns that cannot be fully represented by the DMI alone. The green boxes indicate areas for calculating the DMI as in ref. [1]. Strong and moderate pIOD indices (represented by the S- and M-index, respectively) are calculated from PCs of the EOF of SON SST anomalies over the tropical Indian Ocean for the period of 1900–2099 for each model. **b**, Same as **a**, but for the composite of moderate pIOD (defined as M-index > 1.25 s.d.) in the two shown models. **c**, A total of 20 models (including the two models shown in Fig. 2a,b) produce a nonlinear relationship between PC1 and PC2 with $\alpha \geqq 0.21$; that is, 50% of the observed value (Fig. 1c), and are thus selected for further analysis. A quadratic fit using PC1 and PC2 time-series from the aggregate of the 20 models produces a value of α of 0.31. **d**, Same as **c**, but for the discarded 34 models with $\alpha < 0.21$.

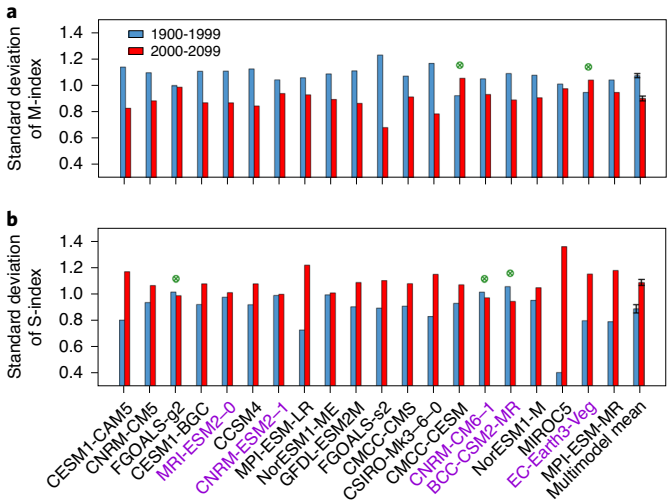

Fig. 3 | Projected opposite response of moderate and strong pIOD SST. The result shows a decrease in moderate pIOD variability but an increase in strong pIOD variability. **a**, A total of 18 out of the 20 selected models (90%) generate a reduction in moderate pIOD variability depicted by the M-index from the present-day (1900–1999, blue bars) to future (2000–2099, red bars) climate, with the exception of two models generating an increase (indicated by green circles). The multimodel mean reduction of 16% is statistically significant above the 95% confidence level according to a bootstrap test. The error bars in the multimodel mean represent the 95% confidence level determined by a bootstrap test. **b**, A total of 17 out of the 20 models (85%) simulate an increase in variability of strong pIOD described by the S-index from the present-day to the future climate, with the exception of three models generating a decrease (indicated by green circles). The multimodel mean increase of 22% is statistically significant above the 95% confidence level according to a bootstrap test. Models from CMIP6 are indicated in purple.

We examine this group of models for assessment of possible change in strong and moderate pIOD events under greenhouse warming. The remaining 34 models produce a far weaker nonlinear PC1 – PC2 relationship (Fig. 2d) and are not used.

Opposite response of the two pIOD regimes to global warming

We compare the standard deviation (s.d.) of the S- and M-index in the present-day (1900–1999) and future (2000–2099) periods. There is an opposite response: a total of 18 out of 20 (that is, 90%) models simulate decreased variability of the M-index (Fig. 3a), whereas a total 17 out of 20 models generate increased variability of the S-index in the future period (red bars, Fig. 3a,b). The ensemble-mean is a decrease of 16% for moderate, but an increase of 22% for strong pIOD variability, each statistically significant above the 95% confidence according to a bootstrap test (see the 'Statistical test' section in the Methods). This is in sharp contrast to the result using the DMI, which shows no statistically significant change in the multimodel mean change (Extended Data Fig. 5).

The decrease in M-index variability translates to a 52% reduction in occurrences of moderate pIOD events with an M-index > 1.25 s.d., as supported by 85% of the selected models (Extended Data Fig. 6a); however, the increase in S-index variability translates to a 66% increase in occurrences of strong pIOD events with an S-index > 1.5 s.d. (Extended Data Fig. 6b)—from one event every 13.3 years in the present-day climate to one event every eight years in the future climate, as supported by 80% of the selected models. The opposite response is despite a lack of frequency change in strong and moderate pIOD events combined (Extended Data Fig. 6a,b), in contrast to a tendency of increased pIOD frequency using DMI (ref. [32]). These results hold using other threshold values (Extended Data Fig. 6c,d). Climate extremes associated with strong pIOD events are thus likely to occur more frequently under greenhouse warming. The 2019 strong pIOD happened to occur in conjunction with a moderate Pacific warm condition[33], leading to more extreme impacts.

Using 30 models simulating a value of α that is at least 33% of the observed value, the intermodel consensus on the change of the two indices is still strong. A total of 27 out of 30 models (90%) simulate a decrease in moderate pIOD variability and a total of 23 out of 30 models (77%) produce an increase in strong pIOD variability, and their ensemble-mean changes are statistically significant (Extended Data Fig. 7). Sensitivity to emission scenarios shows that under RCP4.5, 13 out of 15 (87%) CMIP5 models that simulate a value of α greater than 50% of the observed value generate an increase in S-index variability, and 93% of the models produce a reduction in M-index variability (Extended Data Fig. 8).

Associated mechanisms arising from mean state changes

There is no intermodel relationship between changes in variability or frequency of a strong pIOD event and changes in El Niño

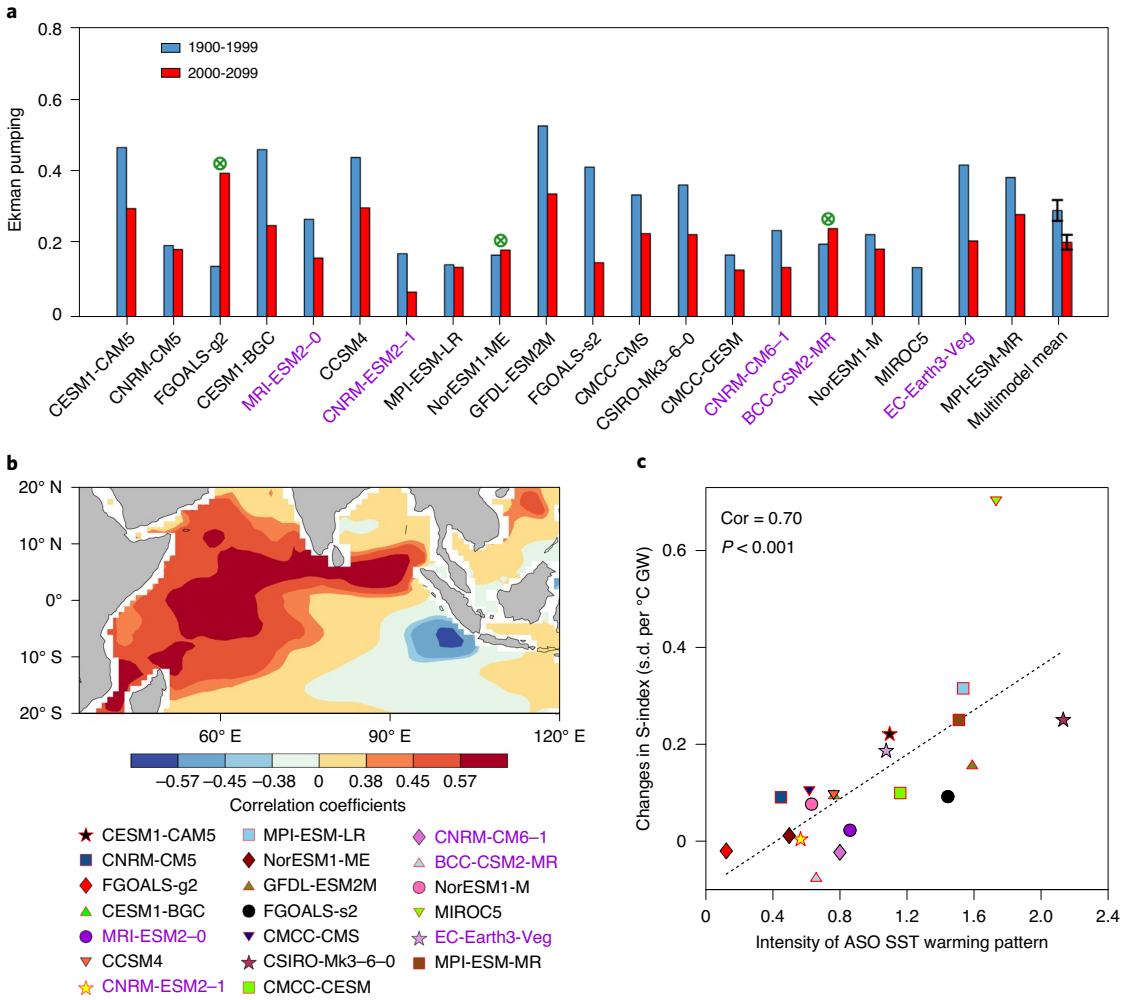

Fig. 4 | Mechanisms for the projected opposite change in moderate and strong pIOD. a, Ekman pumping term during the development phase (August, September, October (ASO)) averaged over the southwestern tropical Indian Ocean (10° S to 0° and 50° E to 80° E) regressed onto the M-index over the present-day (1900–1999, blue bars) and future (2000–2099, red bars) climate in the 20 selected models. A total of 17 out of the 20 selected models (85%) simulate decreased Ekman pumping during future moderate pIOD events. Models that simulate an increase are indicated by green circles. The associated multimodel mean decrease of 30% is statistically significant above the 95% confidence level according to a bootstrap test. Models from CMIP6 are indicated in purple. A time-series of the Ekman pumping term is normalized before regression. The error bar in the multimodel mean represents the 95% confidence level determined by a bootstrap test. **b**, A map of the intermodel correlation coefficients between the ASO warming pattern and the change in the S-index variability. The warming pattern is defined as the change in SST between the future and present-day. The S-index variability change and warming pattern have been scaled by the corresponding increase in global mean SST in each model. Correlation coefficients of ±0.38, ±0.45 and ±0.57 are significant at the 90%, 95% and 99% confidence levels, respectively. **c**, The statistically significant relationship between the intensity of ASO SST warming pattern and the change in s.d. of the S-index is shown, with the correlation (Cor) and its *P*-value indicated. The intensity of the SST warming pattern over 20° S to 20° N and 40° E to 100° E in each model is obtained by regressing onto the multimodel mean SST warming pattern in the same domain; the S-index variability change and warming pattern have been scaled by the corresponding increase in global mean SST in each model, taken as the intensity of global warming (GW).

variability or frequency (Extended Data Fig. 9a,c), which suggests that the changes of strong pIOD are not due to changes in the El Niño. There is a relationship between changes in variability or frequency of a moderate pIOD with changes in El Niño, but the fact that in the majority of models there is an increase in El Niño variability and El Niño frequency in contrast to a decrease in moderate pIOD (Extended Data Fig. 9b,d) rules out changes in the El Niño as the cause.

Instead, the opposite response arises from the mean state changes, featuring faster warming in the western and northern than the eastern and southern tropical Indian Ocean, supported by a trend of equatorial southeasterlies[15–19] and enhanced evaporation in the west (Extended Data Fig. 10). Under greenhouse warming, the lower troposphere warms faster than the surface, such that the response of equatorial easterlies to SST anomalies weakens[16]. Ekman pumping, which is the main forcing for warm anomalies in the tropical western Indian Ocean for moderate pIOD events (Extended Data Fig. 3), weakens in the future climate (Fig. 4a), causing decreased M-index variability. For cold-anomaly-dominated pIOD events (that is, strong pIOD events), the faster mean warming west and northwest of the tropical Indian Ocean[18,19] is conducive to anomalous atmosphere convection there, facilitating anomalous easterlies that extend to the equatorial central and western Indian Ocean, leading to a shallowing thermocline, enhanced equatorial nonlinear zonal and vertical advection, which is in turn conducive to cold anomalies[13,20,27]. Intermodel relationships between warming

trends and changes in S-index variability show that a greater intensity of the warming pattern leads to a great increase in S-index variability (Fig. 4b,c).

Conclusions

Our finding of an opposite response to greenhouse warming—with increased SST variability of strong pIOD events but decreased SST variability of moderate pIOD events—is in stark contrast with previous findings of no consensus using the DMI. Our robust result arises from a separation of the two types of pIOD events that are governed by different dynamics, which provides a physical basis for selecting models used in our pIOD future projections. This projected change of a reduced frequency of moderate pIOD but with more occurrences of stronger pIOD events has far-reaching implications for climate and weather extremes over regions influenced by the pIOD. For example, severe floods in eastern African regions and devastating bushfires in Australia, as seen in 2019, are likely to occur more frequently.

Online content

Any methods, additional references, Nature Research reporting summaries, source data, extended data, supplementary information, acknowledgements, peer review information; details of author contributions and competing interests; and statements of data and code availability are available at https://doi.org/10.1038/s41558-020-00943-1.

Received: 18 March 2020; Accepted: 29 September 2020;
Published online: 30 November 2020

References

1. Saji, N. H., Goswami, B. N., Vinayachandran, P. N. & Yamagata, T. A dipole mode in the tropical Indian Ocean. *Nature* **401**, 360–363 (1999).
2. Webster, P. J., Moore, A. M., Loschnigg, J. P. & Leben, R. R. Coupled ocean–atmosphere dynamics in the Indian Ocean during 1997–98. *Nature* **401**, 356–360 (1999).
3. Schott, F. A., Xie, S.-P. & McCreary Jr, J. P. Indian Ocean circulation and climate variability. *Rev. Geophys.* https://doi.org/10.1029/2007RG000245 (2009).
4. Ummenhofer, C. C. et al. What causes southeast Australia's worst droughts? *Geophys. Res. Lett.* https://doi.org/10.1029/2008GL036801 (2009).
5. Ashok, K., Guan, Z. & Yamagata, T. Influence of the Indian Ocean Dipole on the Australian winter rainfall. *Geophys. Res. Lett.* https://doi.org/10.1029/2003GL017926 (2003).
6. Cai, W., Cowan, T. & Raupach, M. Positive Indian Ocean Dipole events precondition southeast Australia bushfires. *Geophys. Res. Lett.* https://doi.org/10.1029/2009GL039902 (2009).
7. Abram, N. J. et al. Seasonal characteristics of the Indian Ocean Dipole during the Holocene epoch. *Nature* **445**, 299–302 (2007).
8. Abram, N. J., Gagan, M. K., Cole, J. E., Hantoro, W. S. & Mudelsee, M. Recent intensification of tropical climate variability in the Indian Ocean. *Nat. Geosci.* **1**, 849–853 (2008).
9. Behera, S. K. et al. Paramount impact of the Indian Ocean Dipole on the East African short rains: A CGCM study. *J. Clim.* **18**, 4514–4530 (2005).
10. Hashizume, M., Chaves, L. F. & Minakawa, N. Indian Ocean Dipole drives malaria resurgence in East African highlands. *Sci. Rep.* **2**, 269 (2012).
11. Abram, N. J., Gagan, M. K., McCulloch, M. T., Chappell, J. & Hantoro, W. S. Coral Reef Death during the 1997 Indian Ocean Dipole Linked to Indonesian Wildfires. *Science* **301**, 952–955 (2003).
12. Page, S. E. et al. The amount of carbon released from peat and forest fires in Indonesia during 1997. *Nature* **420**, 61–65 (2002).
13. Wang, G., Cai, W., Yang, K., Santoso, A. & Yamagata, T. A unique feature of the 2019 extreme positive Indian Ocean Dipole event. *Geophys. Res. Lett.* https://doi.org/10.1029/2020GL088615 (2020).
14. Richards, L. Brew, N. & Smith, L. *2019–20 Australian Bushfires—Frequently Asked Questions: a Quick Guide* (Parliament of Australia, 2020); https://www.aph.gov.au/About_Parliament/Parliamentary_Departments/Parliamentary_Library/pubs/rp/rp1920/Quick_Guides/AustralianBushfires
15. Cai, W. et al. Projected response of the Indian Ocean Dipole to greenhouse warming. *Nat. Geosci.* **6**, 999–1007 (2013).
16. Zheng, X.-T. et al. Indian Ocean dipole response to global warming in the CMIP5 multimodel ensemble. *J. Clim.* **26**, 6067–6080 (2013).
17. Hui, C. & Zheng, X.-T. Uncertainty in Indian Ocean Dipole response to global warming: the role of internal variability. *Clim. Dyn.* **51**, 3597–3611 (2018).
18. Vecchi, G. A. & Soden, B. J. Global warming and the weakening of the tropical circulation. *J. Clim.* **20**, 4316–4340 (2007).
19. Xie, S.-P. et al. Global warming pattern formation: sea surface temperature and rainfall. *J. Clim.* **23**, 966–986 (2010).
20. Cai, W. et al. Increased frequency of extreme Indian Ocean Dipole events due to greenhouse warming. *Nature* **510**, 254–258 (2014).
21. Weller, E. et al. More-frequent extreme northward shifts of eastern Indian Ocean tropical convergence under greenhouse warming. *Sci. Rep.* **4**, 6087 (2014).
22. Du, Y., Cai, W. & Wu, Y. A new type of the Indian Ocean Dipole since the mid-1970s. *J. Clim.* **26**, 959–972 (2013).
23. Anil, N., Kumar, R., R., M., Sajeev, R. & Saji, P. K. Role of distinct flavours of IOD events on Indian summer monsoon. *Nat. Hazards* **82**, 1317–1326 (2016).
24. Verdon-Kidd, D. C. On the classification of different flavours of Indian Ocean Dipole events. *Int. J. Climatol.* **38**, 4924–4937 (2018).
25. Endo, S. & Tozuka, T. Two flavors of the Indian Ocean Dipole. *Clim. Dyn.* **46**, 3371–3385 (2016).
26. Du, Y., Xie, S.-P., Huang, G. & Hu, K. Role of air–sea interaction in the long persistence of El Niño–induced north Indian Ocean warming. *J. Clim.* **22**, 2023–2038 (2009).
27. Yang, K. et al. Oceanic processes in ocean temperature products key to a realistic presentation of positive Indian Ocean Dipole nonlinearity. *Geophys. Res. Lett.* **46**, e2020GL089396 (2020).
28. Karamperidou, C., Jin, F.-F. & Conroy, J. L. The importance of ENSO nonlinearities in tropical pacific response to external forcing. *Clim. Dyn.* **49**, 2695–2704 (2017).
29. Cai, W. et al. Increased variability of eastern Pacific El Niño under greenhouse warming. *Nature* **564**, 201–206 (2018).
30. Taylor, K. E., Stouffer, R. J. & Meehl, G. A. An overview of CMIP5 and the experiment design. *Bull. Am. Meteorol. Soc.* **93**, 485–498 (2012).
31. Eyring, V. et al. Overview of the coupled model intercomparison project phase 6 (CMIP6) experimental design and organization. *Geosci. Model Dev.* **9**, 1937–1958 (2016).
32. Abram, N. J. et al. Palaeoclimate perspectives on the Indian Ocean Dipole. *Quat. Sci. Rev.* **237**, 106302 (2020).
33. Doi, T., Behera, S. K. & Yamagata, T. Predictability of the super IOD Event in 2019 and its link with El Niño Modoki. *Geophys. Res. Lett.* **47**, e2019GL086713 (2020).

Methods

Data, models and EOF analysis. We use four SST reanalysis products to construct pIOD patterns, covering a common period from 1982 to 2015. Most of these products are produced in a system that specifically considers the impact of subsurface ocean temperature on SST, which is essential for the nonlinear oceanic feedback responsible for the pIOD dominated by cold SST anomalies, that is, strong pIOD episodes. The only exception is OISST, which although not derived from a system explicitly with a subsurface ocean, assimilates weekly observations from different platforms including satellites, ships and buoys. For each of these four data, anomalies are constructed with reference to the mean of the full period, and then detrended. A multiproduct average of the anomalies is then calculated. These products are:

- GODAS (NCEP Global Ocean Data Assimilation System from 1980 to 2019) (ref. [34]);
- ORA-S5 (ECMWF Ocean Reanalysis System 5 from 1979 to 2018) (ref. [35]);
- OISST v2 (NOAA Optimum Interpolation SST version 2 from 1982 to 2019) (ref. [36]);
- SODA3.3.1 (Simple Ocean Data Assimilation version 3.3.1 from 1980 to 2015) (ref. [37]).

To assess the impact of greenhouse warming on pIOD changes, we take outputs from 35 CMIP5 (ref. [30]) and 19 CMIP6 (ref. [31]) coupled global climate models forced with historical anthropogenic and natural forcings, and future greenhouse gases under RCP8.5 for CMIP5 and SSP5–8.5 for CMIP6, covering a 200-year period of 1900–2099 (refs. [30,31]). Monthly anomalies referenced to the climatology of 1900–1999 were constructed and quadratically detrended.

We apply EOF analysis[38] to the SON average of SST anomalies in an equatorial Indian Ocean domain (5° S to 5° N, 40° E to 100° E), which yield the two dominant modes, each with a principal pattern and a PC scaled to unity. The two PC time-series display a nonlinear relationship. A combination of the two EOFs is used to describe the two types of pIOD. Indices of moderate and strong pIOD are described by the M-index $((\mathrm{PC1}-\mathrm{PC2})/\sqrt{2})$ and the S-index $((\mathrm{PC1}+\mathrm{PC2})/\sqrt{2})$, respectively. The two indices separate the pIOD events identified by the DMI into two groups: strong events such as 1994, 1997 and 2006 in the S-index (red curve), and moderate events such as 1982, 1987 and 2015 events (green curve) in the M-index (Fig. 1d). Using these ocean-model-based products identifies the 2006 event as a strong pIOD, as opposed to a moderate one using non-oceanic-based products[20]. Data for the 2019 pIOD event are available in GODAS (ref. [34]), and a pattern regression onto EOF1 and EOF2 shows it to be a strong pIOD, second only to the 1997 event (Fig. 1c).

Heat budget analysis. We examine the surface heat balance of the tropical Indian Ocean, which is expressed as:

$$\partial T^a/\partial t = -\begin{bmatrix} \left(u^a \partial T^a/\partial x + \overline{u}\partial T^a/\partial x + u^a \partial \overline{T}/\partial x\right) \\ +\left(v^a \partial T^a/\partial y + \overline{v}\partial T^a/\partial y + v^a \partial \overline{T}/\partial y\right) \\ +\left(w^a \partial T^a/\partial z + \overline{w}\partial T^a/\partial z + w^a \partial \overline{T}/\partial z\right) \end{bmatrix} + Q + \text{residual} \qquad (1)$$

The variables T, u, v and w are the potential temperature and the zonal, meridional and vertical ocean current velocities, respectively, averaged over the top 50 m (vertical motion over the top 50 m is represented by w at 50 m). The vertical gradient of climatological temperature $(d\overline{T}/dz)$ is taken as the difference between the average over the top 50 m and temperature at 60 m depth. Differential operators, x, y, z, and t represent zonal, meridional and vertical directions, and time, respectively. All variables are from the ECMWF ORA-S5 dataset[35] at a horizontal resolution of 1° latitude by 1° longitude for the period of 1979 to 2018. The rate of change of the mixed-layer temperature $(d\overline{T}/dt)$ is calculated using a centred-difference approximation. The superscript a and overbar denote anomalous and long-term averaged quantities, respectively. The tendency of the surface temperature is balanced by zonal advection of heat by the zonal currents (first bracketed terms on the right-hand side), meridional advection (second bracketed terms), vertical advection (third bracketed terms), the net surface air–sea heat flux (Q) and all other factors not explicitly expressed (residual), such as mixing and diffusion. We examine the heat budget terms averaged over the developing period of IOD events (August to October), which contributes most to the mature SST anomalies. All variables in (1) are linearly detrended.

We first examine the heat budget for the observations in an area average over the equatorial region (10° S to 10° N and 40° E to 100 °E). For strong pIOD events, nonlinear zonal and vertical advection terms are particularly important for generating cold anomalies in the equatorial eastern Indian Ocean[20], and Ekman pumping plays a key role in the generation of warm anomalies (Extended Data Fig. 3a). For moderate pIOD events, Ekman pumping dominates warming (Extended Data Fig. 3a). Inspection of $d\overline{T}/dt$ finds that the region where maximum warming tendency occurs is in the southwestern tropical Indian Ocean (10° S to 0°, 50° E to 80° E, green box of Extended Data Fig. 3b,c). Propagation into the region of downwelling Rossby waves driven by equatorial easterly anomalies associated with a developing pIOD, and their subsequent reflection at the western boundary as downwelling equatorial Kelvin waves induce the broad surface warming[26]. That Ekman pumping in the southwestern tropical Indian Ocean is an important term in the total tendency, and is driven by equatorial easterly anomalies, is reaffirmed by a simple analysis (Extended Data Fig. 3d–f).

We then examine the heat budget for climate models. Data from all models have been interpolated to a horizontal grid of 1°×1° (bilinear interpolation) and a vertical grid with 5 m intervals (linear interpolation). The vertical velocity w at 50 m is used to represent the vertical motion over the upper 50 m layer. Monthly anomalies of w and zonal wind stress are calculated with reference to the 1900–1999 climatology and quadratically detrended. As in observations, nonlinear equatorial zonal and vertical advection are dominant in forcing strong pIOD events, and these terms increase under greenhouse warming[20].

For the present-day and future model climate, we take the climatological mean temperature $(\overline{T})$ as the average over the 1900–1999 and 2000–2099 periods, respectively. There is a general decrease in the response of zonal wind stress to SST in the equatorial eastern Indian Ocean, as a consequence of a more stable atmosphere that results from a faster warming in the lower troposphere than at the surface under greenhouse warming[16]. The associated decrease in variability of zonal wind stress anomalies, which drive Ekman pumping that dominates moderate pIOD events, leads to decreased variability of moderate pIOD in the future climate. In the 20 selected models, 19 models generate a future decrease of w variability in the development phase over the southwestern tropical Indian Ocean (green box, Extended Data Fig. 3b). A bootstrap test finds that the multimodel mean decrease of 21% is statistically significant. By contrast, for strong pIOD events, equatorial nonlinear zonal and vertical advection occurs more frequently as a consequence of faster warming in the northwestern equatorial Indian Ocean under greenhouse warming[20].

Nonlinear dynamics and model selection. During strong pIOD events, the initial cooling grows such that it extends northward first and then westward along the equator, triggering the equatorial nonlinear ocean–atmosphere feedback: an equatorial west-minus-east zonal SST gradient drives easterly anomalies, leading to nonlinear vertical and nonlinear zonal advection extending the cold anomalies along the equatorial eastern Indian Ocean[13,20,27], as represented by PC2. The dynamics that govern PC2 and the associated pattern depends nonlinearly on cold anomalies presented in PC1 that first grow northwest towards and then westward along the equator, such that $\mathrm{PC2}(t)=\alpha[\mathrm{PC1}(t)]^2+\beta\mathrm{PC1}(t)+\gamma$. For the observed, the value of α is 0.42 (Fig. 1c); a greater value of α means a clearer separation of the two types of the pIOD events.

Not all models produce the nonlinear dynamics that separate the strong and moderate pIOD events, and most models produce a weaker nonlinearity than seen in the observed. We select 20 CMIP5 and CMIP6 models that simulate an α, calculated over the 200 years, greater than half of the observed value. The 20 selected models together yield a mean α amplitude of 0.31 (Fig. 2c). A total of 30 models simulate an α greater than 33% of the observed value and we use this group to test the sensitivity of our results.

Statistical significance test. A bootstrap method[39] is used to examine whether the increased S-index variance and decreased M-index variance are statistically significant. The 20 s.d. values of the S- and M-index in the present-day climate (1900–1999) from the 20 selected models are resampled randomly to construct 10,000 realizations of the mean standard deviation. In this random resampling process, a model is allowed to be selected again. The s.d. of the 10,000 interrealizations of mean s.d. in the present-day climate is 0.0312 for the S-index (0.0157 for the M-index). The same test is carried out for the future climate (2000–2099) and the s.d. of the interrealization is 0.0212 for the S-index (0.0185 for the M-index). The increased s.d. for the S-index (or decreased s.d. for the M-index) in the future period is greater than the sum of the two s.d. values, indicating statistical significance above the 95% confidence level.

Data availability

Data relevant to the paper can be downloaded from websites listed below:
OISST v2 at https://www.esrl.noaa.gov/psd/data/gridded/data.noaa.oisst.v2.html;
ORA-S5 at https://icdc.cen.uni-hamburg.de/daten/reanalysis-ocean/easy-init-ocean/ecmwf-oras5.html;
SODA3.3.1 at https://www2.atmos.umd.edu/~ocean/index_files/soda3.3.1_mn_download.htm;
GODAS at https://www.esrl.noaa.gov/psd/data/gridded/data.godas.html;
CMIP5 database at http://www.ipcc-data.org/sim/gcm_monthly/AR5/;
CMIP6 database at https://esgf-node.llnl.gov/projects/cmip6/;
19 CMIP6 models are used in this study, including: MRI-ESM2–0 (refs. [40,41]); CNRM-ESM2–1 (refs. [42,43]); CNRM-CM6–1 (refs. [44,45]); BCC-CSM2-MR (refs. [46,47]); EC-Earth3-Veg (refs. [48,49]); NorESM2-LM (refs. [50,51]); MIROC6 (refs. [52,53]); CESM2 (refs. [54,55]); CAMS-CSM1-0 (refs. [56,57]); CESM2-WACCM (refs. [58,59]); MIROC-ES2L (refs. [60,61]); IPSL-CM6A-LR (refs. [62,63]); INM-CM4-8 (refs. [64,65]); INM-CM5-0 (refs. [66,67]); CanESM5 (refs. [68,69]); MPI-ESM1-2-LR (refs. [70,71]); UKESM1-0-LL (refs. [72,73]); MCM-UA-1-0 (refs. [74,75]); GFDL-CM4 (refs. [76,77]).

Code availability

Codes for calculating EOF, the parameter $|\alpha|$ can be downloaded from https://drive.google.com/open?id=1d2R8wKpFNW-vMIfoJsbqIGPIBd9Z_8rj.

References

34. Behringer, D. & Xue, Y. Evaluation of the global ocean data assimilation system at NCEP: the Pacific Ocean. In *Eighth Symposium on Integrated Observing and Assimilation Systems for Atmosphere, Oceans, and Land Surface* (Americal Meteorological Society, 2004).
35. Zuo, H., Balmaseda, M. A., Tietsche, S., Mogensen, K. & Mayer, M. The ECMWF operational ensemble reanalysis–analysis system for ocean and sea ice: a description of the system and assessment. *Ocean Sci.* **15**, 779–808 (2019).
36. Reynolds, R. W., Rayner, N. A., Smith, T. M., Stokes, D. C. & Wang, W. An improved in situ and satellite SST analysis for climate. *J. Clim.* **15**, 1609–1625 (2002).
37. Carton, J. A., Chepurin, G. A. & Chen, L. SODA3: A new ocean climate reanalysis. *J. Clim.* **31**, 6967–6983 (2018).
38. Lorenz, E. N. *Empirical Orthogonal Functions and Statistical Weather Prediction* Statistical Forecast Project Report 1 (Department of Meteorology, Massachusetts Institute of Technology, 1956).
39. Austin, P. C. & Tu, J. V. Bootstrap methods for developing predictive models. *The American Statistician* **58**, 131–137 (2004).
40. Yukimoto, S. et al. *MRI MRI-ESM2.0 Model Output Prepared for CMIP6 CMIP Historical* Version 20200102 (Earth System Grid Federation, 2019); https://doi.org/10.22033/ESGF/CMIP6.6842
41. Yukimoto, S. et al. *MRI MRI-ESM2.0 Model Output Prepared for CMIP6 ScenarioMIP ssp585* Version 20200102 (Earth System Grid Federation, 2019); https://doi.org/10.22033/ESGF/CMIP6.6929
42. Seferian, R. *CNRM-CERFACS CNRM-ESM2-1 Model Output Prepared for CMIP6 CMIP Historical* Version 20200102 (Earth System Grid Federation, 2018); https://doi.org/10.22033/ESGF/CMIP6.4068
43. Voldoire, A. *CNRM-CERFACS CNRM-ESM2-1 Model Output Prepared for CMIP6 ScenarioMIP ssp585* Version 20200102 (Earth System Grid Federation, 2019); https://doi.org/10.22033/ESGF/CMIP6.4226
44. Voldoire, A. *CMIP6 Simulations of the CNRM-CERFACS Based on CNRM-CM6-1 Model for CMIP Experiment Historical* Version 20200102 (Earth System Grid Federation, 2018); https://doi.org/10.22033/ESGF/CMIP6.4066
45. Voldoire, A. *CNRM-CERFACS CNRM-CM6-1 Model Output Prepared for CMIP6 ScenarioMIP ssp585* Version 20200102 (Earth System Grid Federation, 2019); https://doi.org/10.22033/ESGF/CMIP6.4224
46. Wu, T. et al. *BCC BCC-CSM2MR Model Output Prepared for CMIP6 CMIP Historical* Version 20200102 (Earth System Grid Federation, 2018); https://doi.org/10.22033/ESGF/CMIP6.2948
47. Xin, X. et al. *BCC BCC-CSM2MR Model Output Prepared for CMIP6 ScenarioMIP ssp585* Version 20200102 (Earth System Grid Federation, 2019); https://doi.org/10.22033/ESGF/CMIP6.3050
48. EC-Earth Consortium (EC-Earth) *EC-Earth-Consortium EC-Earth3-Veg Model Output Prepared for CMIP6 CMIP Historical* Version 20200102 (Earth System Grid Federation, 2019); https://doi.org/10.22033/ESGF/CMIP6.4706
49. EC-Earth Consortium (EC-Earth) *EC-Earth-Consortium EC-Earth3-Veg Model Output Prepared for CMIP6 ScenarioMIP ssp585* Version 20200102 (Earth System Grid Federation, 2019); https://doi.org/10.22033/ESGF/CMIP6.4914
50. Seland, Ø. et al. *NCC NorESM2-LM Model Output Prepared for CMIP6 CMIP Historical* Version 20200102 (Earth System Grid Federation, 2019); https://doi.org/10.22033/ESGF/CMIP6.8036
51. Seland, Ø. et al. *NCC NorESM2-LM Model Output Prepared for CMIP6 ScenarioMIP ssp585* Version 20200102 (Earth System Grid Federation, 2019); https://doi.org/10.22033/ESGF/CMIP6.8319
52. Tatebe, H. & Watanabe, M. *MIROC MIROC6 Model Output Prepared for CMIP6 CMIP Historical* Version 20200102 (Earth System Grid Federation, 2018); https://doi.org/10.22033/ESGF/CMIP6.5603
53. Shiogama, H., Abe, M. & Tatebe, H. *MIROC MIROC6 Model Output Prepared for CMIP6 ScenarioMIP ssp585* Version 20200102 (Earth System Grid Federation, 2019); https://doi.org/10.22033/ESGF/CMIP6.5771
54. Danabasoglu, G. *NCAR CESM2 Model Output Prepared for CMIP6 CMIP Historical* Version 20200102 (Earth System Grid Federation, 2019); https://doi.org/10.22033/ESGF/CMIP6.7627
55. Danabasoglu, G. *NCAR CESM2 Model Output Prepared for CMIP6 ScenarioMIP ssp585* Version 20200102 (Earth System Grid Federation, 2019); https://doi.org/10.22033/ESGF/CMIP6.7768
56. Rong, X. C. A. M. S. CAMS_CSM1.0 *Model Output Prepared for CMIP6 CMIP Historical* Version 20200102 (Earth System Grid Federation, 2019); https://doi.org/10.22033/ESGF/CMIP6.9754
57. Rong, X. *CAMS CAMS-CSM1.0 Model Output Prepared for CMIP6 ScenarioMIP ssp585* Version 20200102 (Earth System Grid Federation, 2019); https://doi.org/10.22033/ESGF/CMIP6.11052
58. Danabasoglu, G. *NCAR CESM2-WACCM Model Output Prepared for CMIP6 CMIP Historical* Version 20200102 (Earth System Grid Federation, 2019); https://doi.org/10.22033/ESGF/CMIP6.10071
59. Danabasoglu, G. *NCAR CESM2-WACCM Model Output Prepared for CMIP6 ScenarioMIP ssp585* Version 20200102 (Earth System Grid Federation, 2019); https://doi.org/10.22033/ESGF/CMIP6.10115
60. Hajima, T. et al. *MIROC MIROC-ES2L Model Output Prepared for CMIP6 CMIP Historical* Version 20200102 (Earth System Grid Federation, 2019); https://doi.org/10.22033/ESGF/CMIP6.5602
61. Tachiiri, K. et al. *MIROC MIROC-ES2L Model Output Prepared for CMIP6 ScenarioMIP ssp585* Version 20200102 (Earth System Grid Federation, 2019); https://doi.org/10.22033/ESGF/CMIP6.5770
62. Boucher, O. et al. *IPSL IPSL-CM6A-LR Model Output Prepared for CMIP6 CMIP Historical* Version 20200102 (Earth System Grid Federation, 2018); https://doi.org/10.22033/ESGF/CMIP6.5195
63. Boucher, O. et al. *IPSL IPSL-CM6A-LR Model Output Prepared for CMIP6 ScenarioMIP ssp585* Version 20200102 (Earth System Grid Federation, 2019); https://doi.org/10.22033/ESGF/CMIP6.5271
64. Volodin, E. et al. *INM INM-CM4-8 Model Output Prepared for CMIP6 CMIP Historical Version 20200102* (Earth System Grid Federation, 2019); https://doi.org/10.22033/ESGF/CMIP6.5069
65. Volodin, E. et al. *INd INM-CM4-8 Model Output Prepared for CMIP6 ScenarioMIP ssp585* Version 20200102 (Earth System Grid Federation, 2019); https://doi.org/10.22033/ESGF/CMIP6.12337
66. Volodin, E. et al. *INM INM-CM5-0 Model Output Prepared for CMIP6 CMIP Historical* Version 20200102 (Earth System Grid Federation, 2019); https://doi.org/10.22033/ESGF/CMIP6.5070
67. Volodin, E. et al. *INM INM-CM5-0 Model Output Prepared for CMIP6 ScenarioMIP ssp585* Version 20200102 (Earth System Grid Federation, 2019); https://doi.org/10.22033/ESGF/CMIP6.12338
68. Swart, N. C. et al. *CCCma CanESM5 Model Output Prepared for CMIP6 CMIP Historical* Version 20200102 (Earth System Grid Federation, 2019); https://doi.org/10.22033/ESGF/CMIP6.3610
69. Swart, N. C. et al. *CCCma CanESM5 Model Output Prepared for CMIP6 ScenarioMIP ssp585* Version 20200102 (Earth System Grid Federation, 2019); https://doi.org/10.22033/ESGF/CMIP6.3696
70. Wieners, K.-H. et al. *MPI-M MPI-ESM1.2-LR Model Output Prepared for CMIP6 CMIP Historical* Version 20200102 (Earth System Grid Federation, 2019); https://doi.org/10.22033/ESGF/CMIP6.6595
71. Wieners, K.-H. et al. *MPI-M MPI-ESM1.2-LR Model Output Prepared for CMIP6 ScenarioMIP ssp585* Version 20200102 (Earth System Grid Federation, 2019); https://doi.org/10.22033/ESGF/CMIP6.6705
72. Tang, Y. et al. *MOHC UKESM1.0-LL Model Output Prepared for CMIP6 CMIP Historical* Version 20200102 (Earth System Grid Federation, 2019); https://doi.org/10.22033/ESGF/CMIP6.6113
73. Good, P. et al. *MOHC UKESM1.0-LL Model Output Prepared for CMIP6 ScenarioMIP ssp585* Version 20200102 (Earth System Grid Federation, 2019); https://doi.org/10.22033/ESGF/CMIP6.6405
74. Stouffer, R. *UA MCM-UA-1-0 Model Output Prepared for CMIP6 CMIP Historical* Version 20200102 (Earth System Grid Federation, 2019); https://doi.org/10.22033/ESGF/CMIP6.8888
75. Stouffer, R. *UA MCM-UA-1-0 Model Output Prepared for CMIP6 ScenarioMIP ssp585* Version 20200102 (Earth System Grid Federation, 2019); https://doi.org/10.22033/ESGF/CMIP6.13901
76. Guo, H. et al. *NOAA-GFDL GFDL-CM4 Model Output* Version 20200102 (Earth System Grid Federation, 2018); https://doi.org/10.22033/ESGF/CMIP6.1402
77. Guo, H. et al. *NOAA-GFDL GFDL-CM4 Model Output Prepared for CMIP6 ScenarioMIP* Version 20200102 (Earth System Grid Federation, 2018); https://doi.org/10.22033/ESGF/CMIP6.9242

Acknowledgements

This work is supported by National Key R&D Program of China (grant no. 2018YFA0605700). L.W. is supported by the National Natural Science Foundation of China (NSFC) projects (grant nos. 41490643, 41490640, U1606402 and 41521091). W.C., G.W., A.S. and B.N. are supported by CSHOR and the Earth System and Climate Change Hub of the Australian Government's National Environment Science Program. CSHOR is a joint research Center for Southern Hemisphere Oceans Research between QNLM and CSIRO. G.H. is supported by NSFC (grant nos. 41831175 and 91937302), CAS XDA20060501 and COMS2019Q03. K.Y. is supported by China Postdoctoral Science Foundation (grant no. 2018M640168) and a scholarship from China Scholarship Council. We acknowledge the World Climate Research Programme's Working Group on Coupled Modelling, which is responsible for CMIP, and we thank the climate modeling groups for producing and making available their model output. For CMIP, the US Department of Energy's Program for Climate Model Diagnosis and Intercomparison provides coordinating support and led development of software infrastructure in partnership with the Global Organization for Earth System Science Portals. We are grateful to the reanalysis groups for making the datasets publicly available.

Author contributions

W.C. conceived the study and wrote the initial manuscript in discussion with K.Y. K.Y. performed all analysis and generated final figures. All authors contributed to interpreting results, discussion of the associated dynamics and improvement of this paper.

Competing interests

The authors declare no competing interests.

Additional information

Extended data is available for this paper at https://doi.org/10.1038/s41558-020-00943-1.

Correspondence and requests for materials should be addressed to W.C. or L.W.

Peer review information *Nature Climate Change* thanks Jasti Chowdary and the other, anonymous, reviewer(s) for their contribution to the peer review of this work.

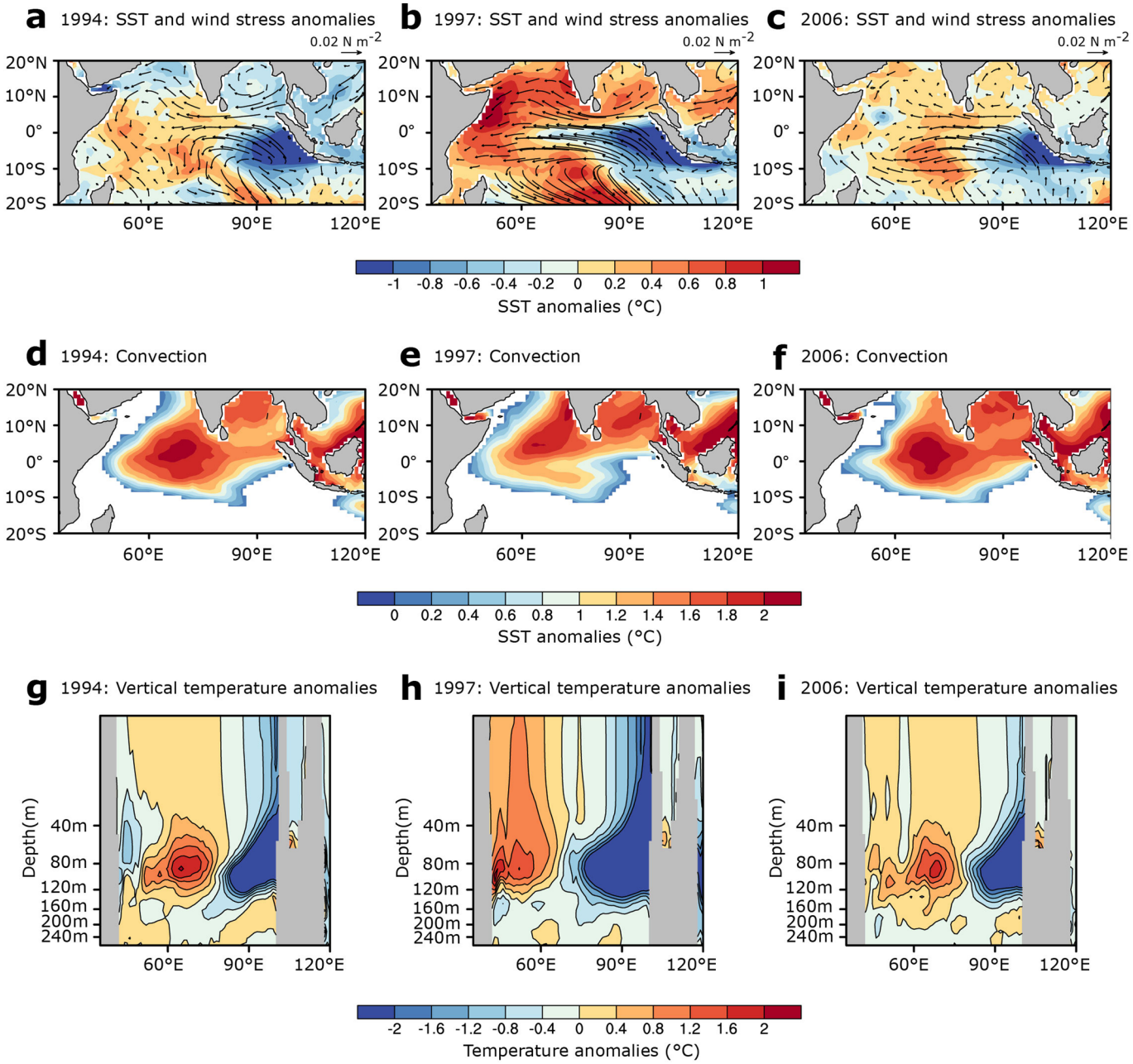

Extended Data Fig. 1 | Characteristics of strong pIOD events. a–c, SON SST anomalies (°C, color shading) and wind stress anomalies (N m^{-2}, vectors) for the 1994, 1997, and 2006 strong pIOD event, respectively. The pattern is dominated by strong cooling in the equatorial eastern Indian Ocean. Strong equatorial easterly anomalies extend to the central-western Indian Ocean. The anomalies are referenced to the average over the 1982–2015 period. **d–f**, SON SST anomalies (in °C) relative to the SST threshold for tropical convection, defined as the SON SST average over 20°S to 20°N, for the 1994, 1997, and 2006 strong pIOD event, respectively. Areas with SST lower than the convection threshold have been masked; there is a large area of suppressed convection in the equatorial eastern Indian Ocean. **g–i**, Equatorial vertical potential temperature anomalies (in °C) over SON of 1994, 1997, and 2006, respectively. The equatorial vertical potential temperature is calculated as the average between 2.5°S to 2.5°N. Strong equatorial cooling is seen in the eastern Indian Ocean. Vertical potential temperature and wind stress data are from ORA-S5.

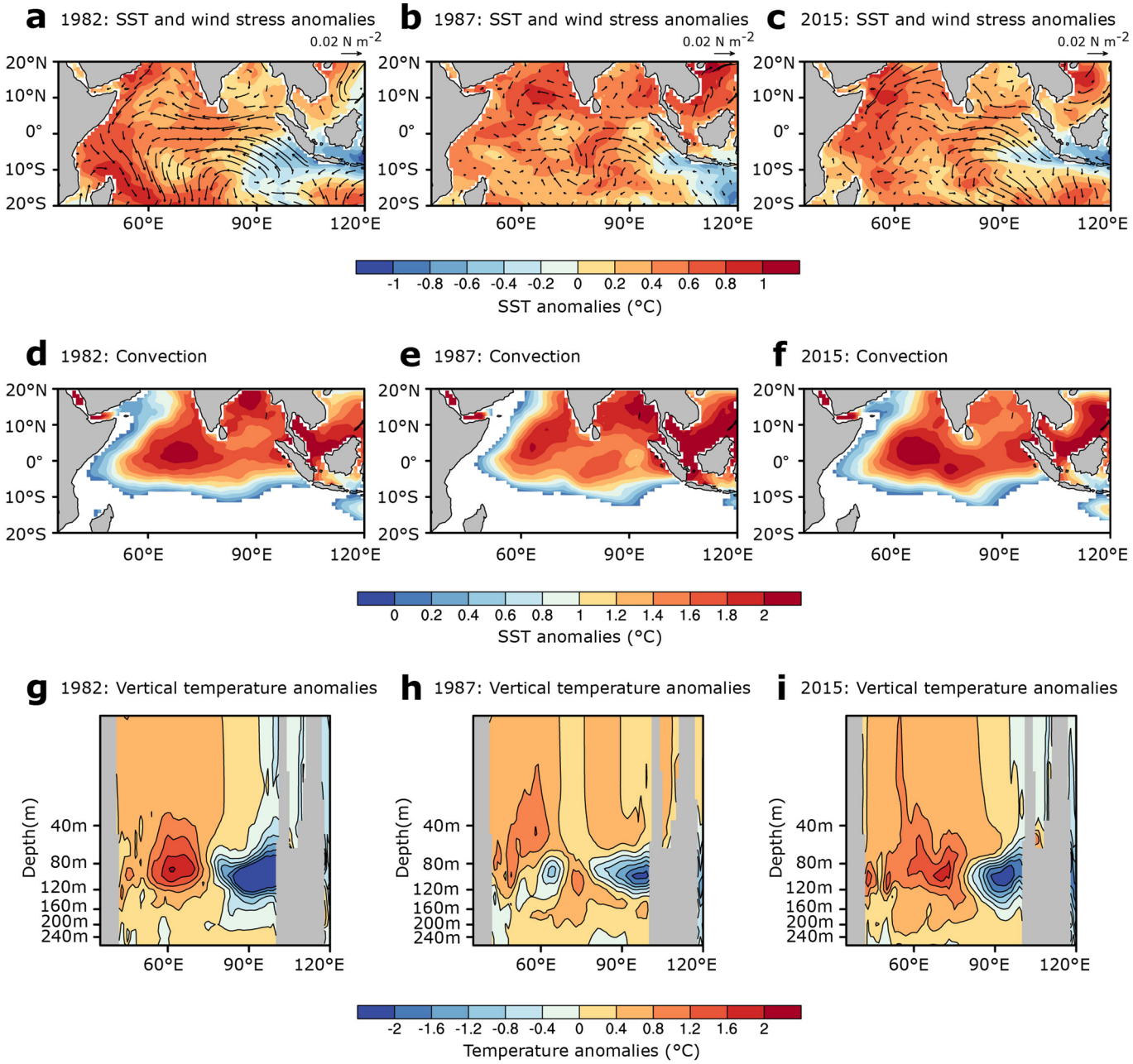

Extended Data Fig. 2 | Characteristics of moderate pIOD events. a–c, SON SST anomalies (°C, color shading) and wind stress anomalies (N m^{-2}, vectors) for the 1982, 1987, and 2015 moderate pIOD event, respectively. The pattern is dominated by a broad-scale warming over the western Indian Ocean. Easterly anomalies are confined to the equatorial central-eastern Indian Ocean. The anomalies are referenced to the average over the 1982–2015 period. **d–f**, SON SST anomalies (in °C) relative to SST threshold for tropical convection, defined as SON SST average over 20°S to 20°N for 1982, 1987, and 2015 moderate pIOD event, respectively. Areas with SST lower than the convection threshold have been masked; there is a small area of suppressed convection in the equatorial southeastern Indian Ocean. **g–i**, Equatorial vertical potential temperature anomalies (in °C) over SON of 1982, 1987, and 2015, respectively. The equatorial vertical potential temperature is calculated as the average between 2.5°S to 2.5°N. There is a general lack of cooling in the equatorial eastern Indian Ocean as cooling occurs only off Sumatra-Java. Vertical potential temperature and wind stress data are from ORA-S5.

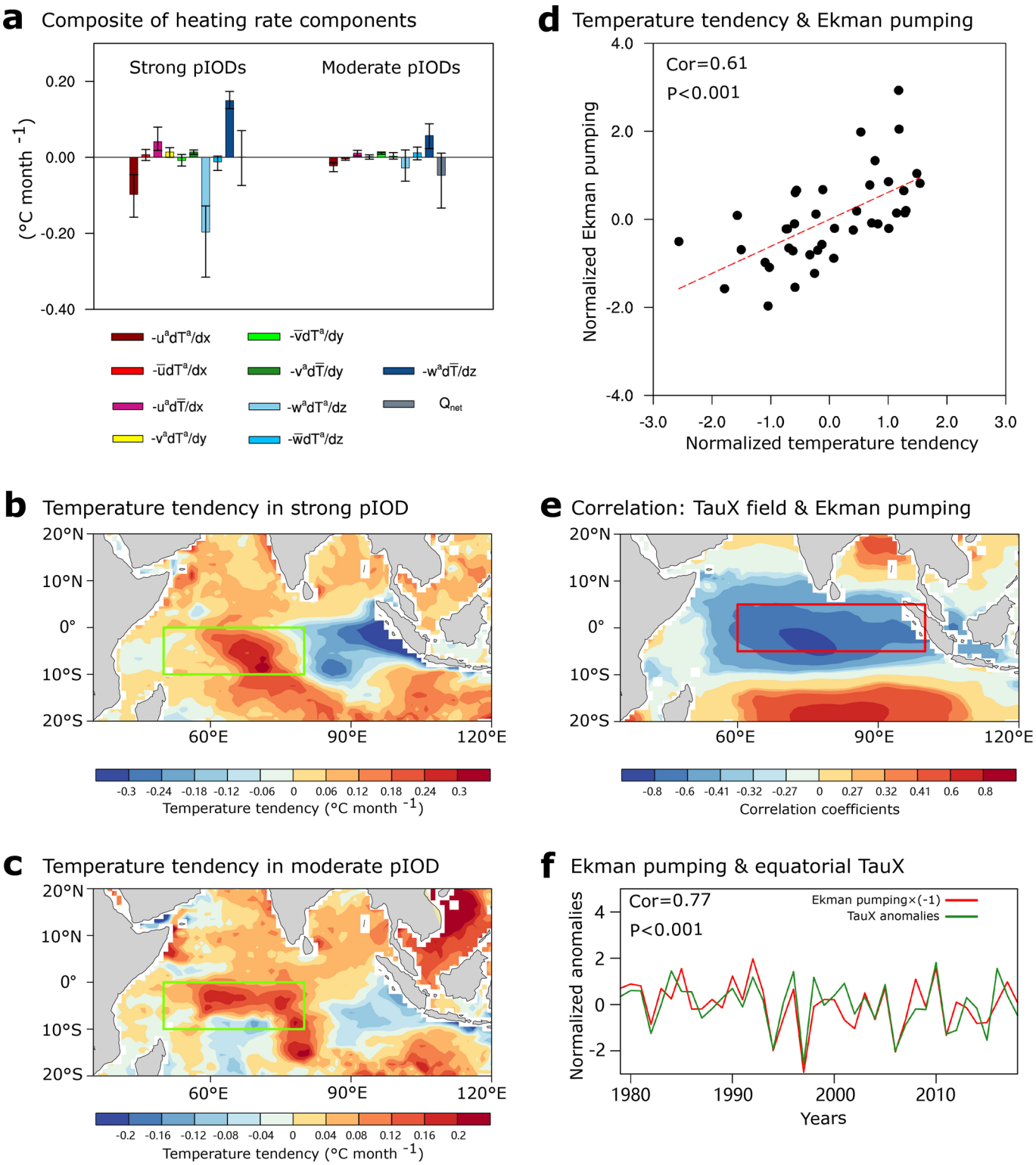

Extended Data Fig. 3 | Heat budget analysis based on observations. a, Composite of heat budget terms over the equatorial Indian Ocean (10°S–10°N, 40°E–100°E) in August-September-October (ASO). The uncertainty bar on each composite represents the range over the three strong or three moderate pIOD events. **b**, **c**, Composite of ASO temperature tendency during strong and moderate pIOD events. The green box marks the area where the main warm temperature tendency is located over the southwestern Indian Ocean (10°S–0°, 50°E–80°E). **d**, Relationship between normalized temperature tendency and the Ekman pumping term in ASO averaged over the main warming area in the southwestern Indian ocean (10°S–0°, 50°E–80°E, green box in c), with statistical properties shown. **e**, Map of ASO correlation coefficients between the Ekman pumping term averaged over 10°S–0°, 50°E–80°E and zonal wind stress (TauX) anomalies. Correlation coefficients of ±0.27, ±0.32, ±0.41 are statistically significant at the 90%, 95%, and 99% confidence levels, respectively. The area indicated by the red box is used to calculate the average zonal wind stress anomalies. **f**, Time series of normalized ASO Ekman pumping term averaged over the western Indian Ocean (10°S–0°, 50°E–80°E) (red curve) and zonal wind stress (TauX) anomalies averaged over the equatorial Indian Ocean (5°S–5°N, 60°E–100°E, red box in e) (green curve). The Ekman pumping term has been multiplied by –1 for plotting. The data used in this figure are from ORA-S5 for the period of 1979–2018.

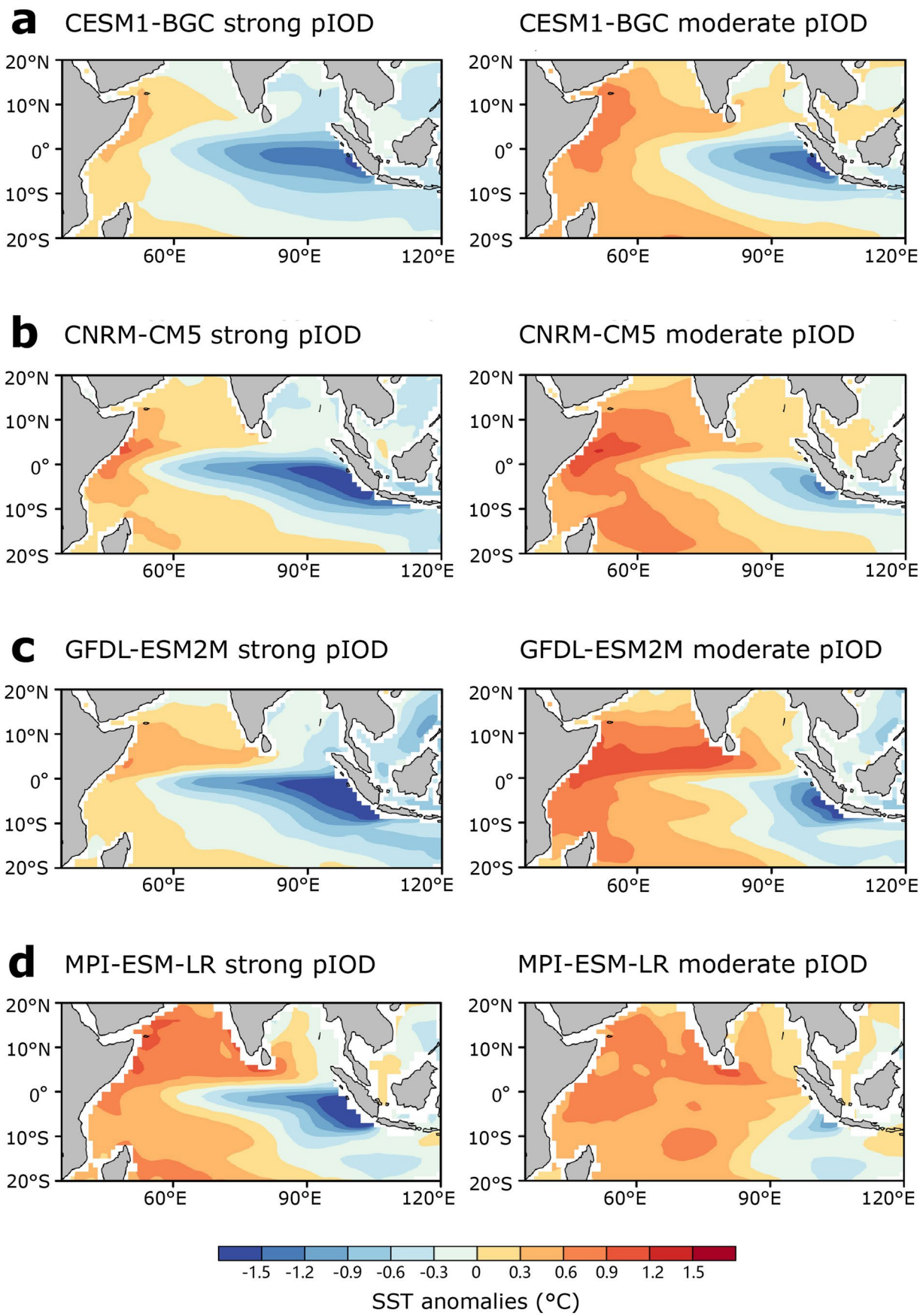

Extended Data Fig. 4 | Anomaly patterns of strong and moderate pIOD in some selected models. A composite of SON SST anomalies (°C) for strong pIOD with an S-index>1.5 s.d. and moderate pIOD with an M-index>1.25 s.d. in **a** CESM1-BGC, **b** CNRM-CM5, **c** GFDL-ESM2M, **d** MPI-ESM-LR. Left panels show strong pIOD and right panels show moderate pIOD. These show that anomaly patterns can be rather different from one model to another.

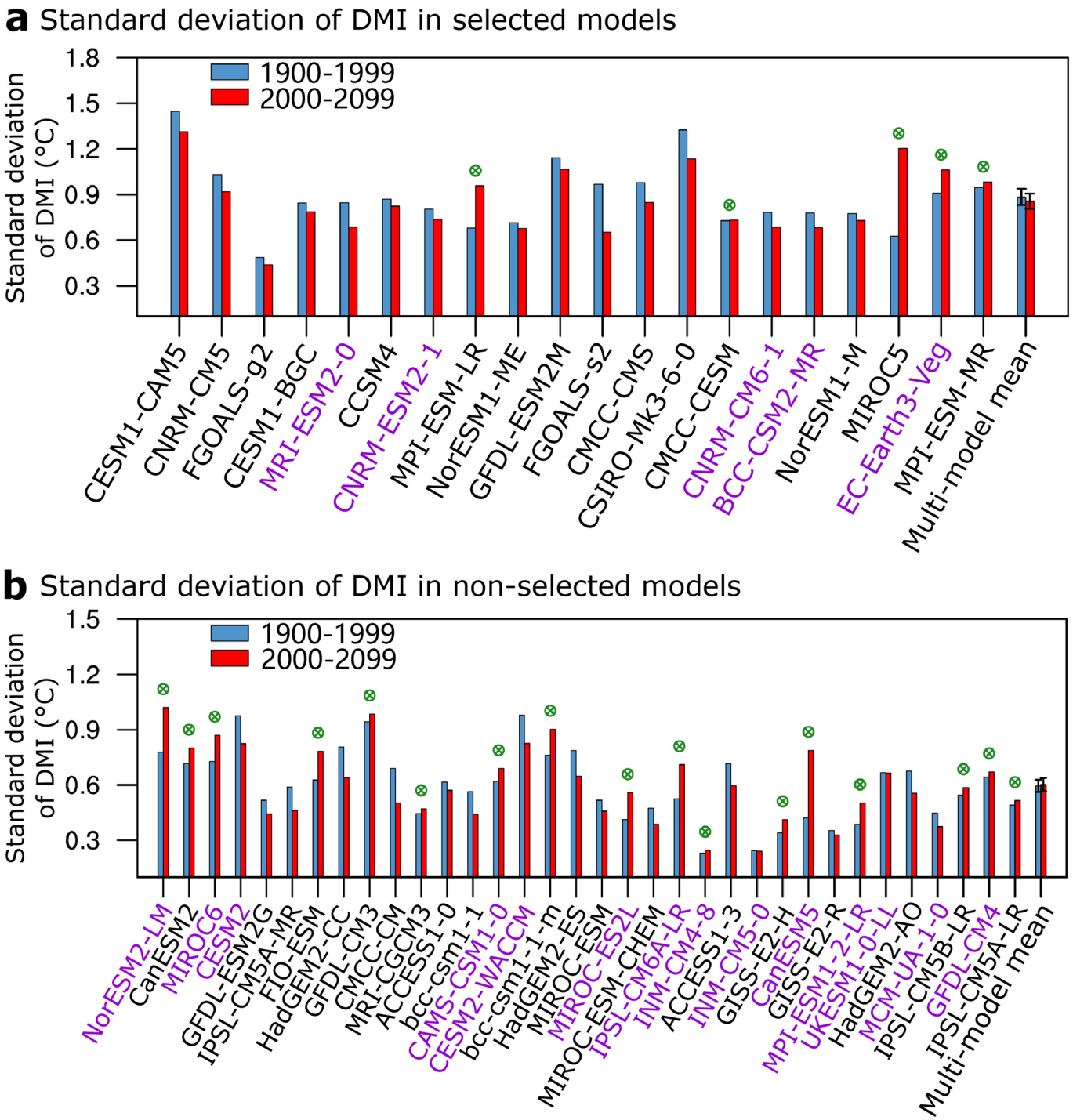

Extended Data Fig. 5 | Uncertainty in projected pIOD SST using the DMI. a, Comparison of the standard deviation of the DMI in the present-day (1900–1999) and future (2000–2099) climate in 20 models that simulate a nonlinear coefficient α greater than 50% of the observed in the quadratic fit between the first two principal components (PC1 and PC2) from EOF analysis on SON SST anomalies, $PC2(t) = \alpha\,[PC1(t)]^2 + \beta\,PC1(t) + \gamma$. Although a total of 15 out of the 20 selected models simulate lower DMI variability in the future period (red bars) than in the present-day climate (blue bars), the multi-model mean decrease is not statistically significant. The error bar represents the 95% confidence level. Models that simulate an increase in variability are indicated by green circles. Models from CMIP6 are shown in purple. **b**, Same as **a**, but for 34 models that simulate an α smaller than 50% of the observed value. A total of 17 out of the 34 models (50%) simulate smaller variability in the DMI in the future period than in the present-day period. There is no inter-model consensus, and the multi-model mean change is not statistically significant.

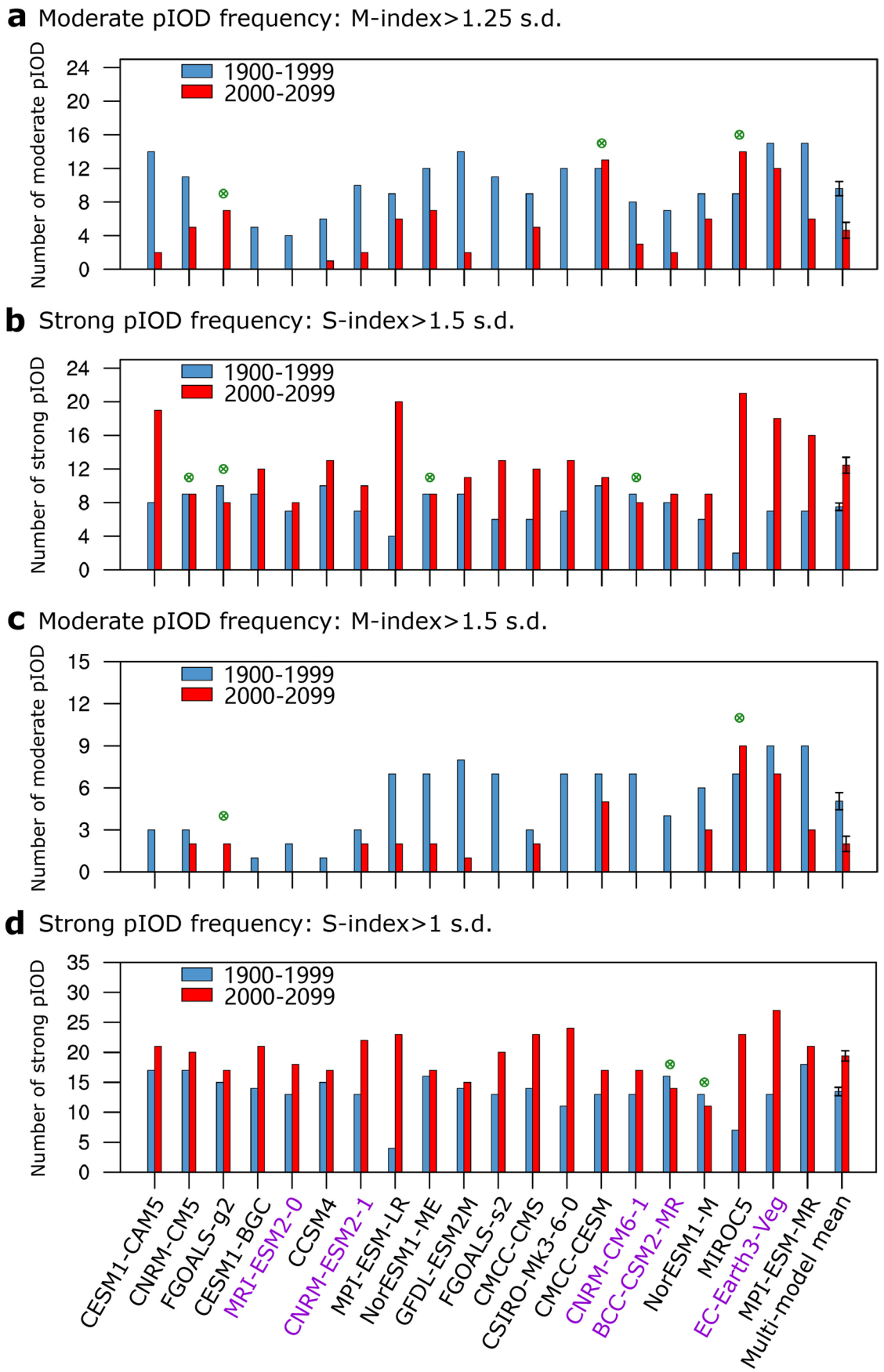

Extended Data Fig. 6 | See next page for caption.

Extended Data Fig. 6 | Projected change in pIOD frequency. a, Moderate and **b**, strong pIOD using a threshold of M-index>1.25 s.d. and S-index>1.5 s.d., respectively. Shown is the comparison of frequency (events per 100 years) in the present-day (1900–1999) and future (2000–2099) climate in the 20 selected models, that is, with an α greater than 50% of the observed value. A total of 17 out of the 20 models (85%) simulate a decreased frequency in moderate pIOD events, with a statistically significant decrease of 52% in the multi-model mean, from 9.60 events per 100 years in the present-day (blue bars) to 4.65 events per 100 years (red bars) in the future climate. By contrast, a total of 16 out of the 20 models (80%) simulate an increased frequency in strong pIOD events, with a statistically significant increase of 66% in the multi-model average, from 7.5 events per 100 years in the present-day (blue bars) to 12.45 events per 100 years (red bars) in the future climate. Models that simulate an opposite change to the multi-model mean are indicated by green circles. **c**, Same as **a**, but using a threshold of M-index>1.5 s.d. A total of 18 out of the 20 selected models (90%) simulate a decreased frequency in moderate pIOD events, with a statistically significant decrease of 60% in the multi-model ensemble mean. **d**, Same as **b**, but using a threshold of S-index>1 s.d. A total of 18 out of the 20 models (90%) simulate an increased frequency in strong pIOD, with a statistically significant increase of 44% in the multi-model ensemble mean. Models from CMIP6 are indicated in purple.

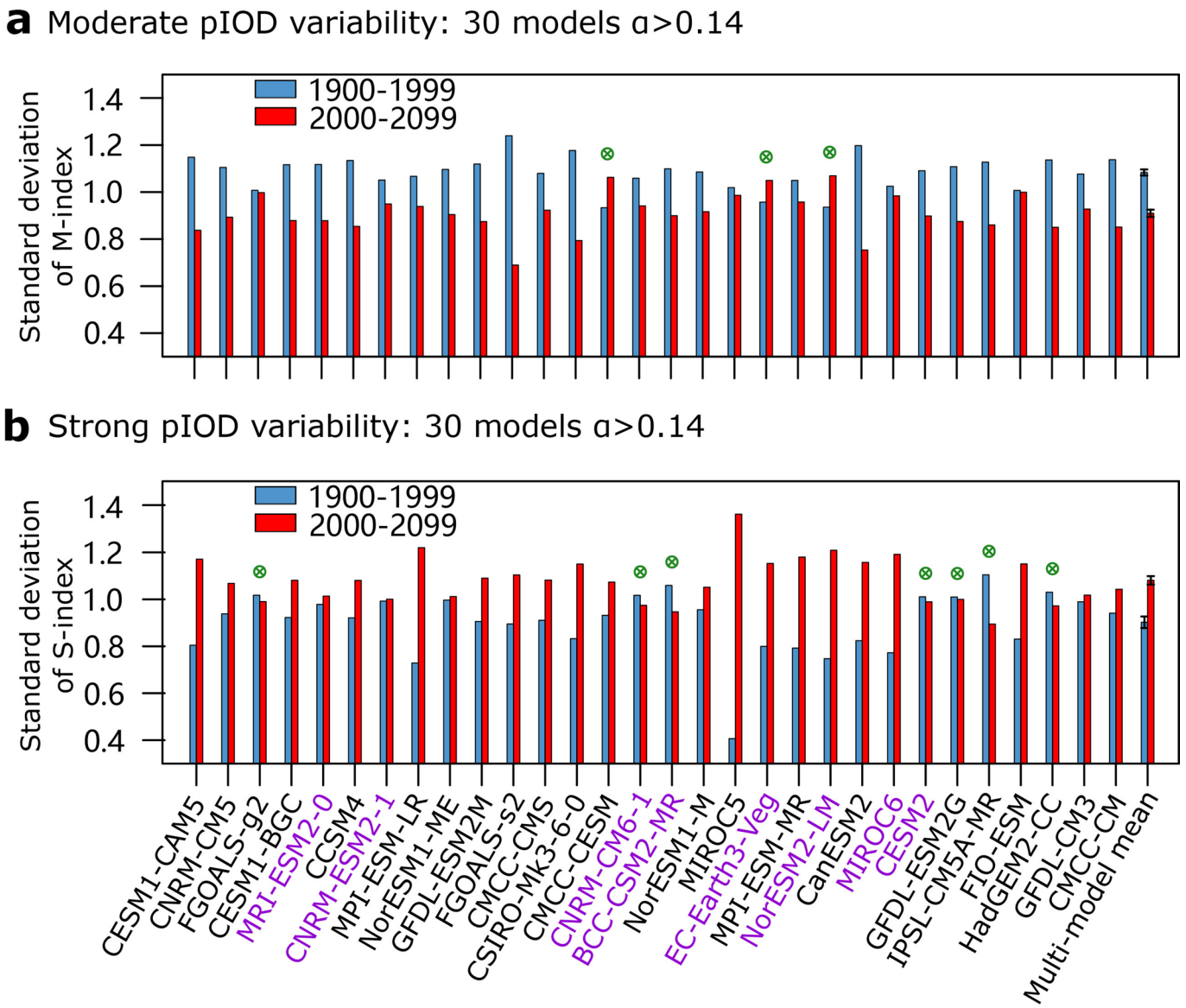

Extended Data Fig. 7 | Sensitivity of projected changes in pIOD variability to model selections. a, **b**, Comparison of variability of the moderate pIOD (M-index) and strong pIOD (S-index), respectively, in the present-day (1900–1999) and future (2000–2099) climate in 30 models that simulate a nonlinear coefficient α greater than 33.3% of the observed value. In **a**, a total of 27 out of the 30 models (90%) simulate a decrease in M-index variability in the future period (red bars) from that in the present-day period (blue bars). This leads to a multi-model mean decrease of 17%, statistically significant above the 95% confidence level, as indicated by the error bars. In **b**, a total of 23 out of the 30 selected models (77%) simulate an increase in S-index variability in the future climate, with a multi-model mean increase of 19%, statistically significant above the 95% confidence level. Models from CMIP6 are indicated in purple. Models that simulate an opposite change to the multi-model mean are indicated by green circles.

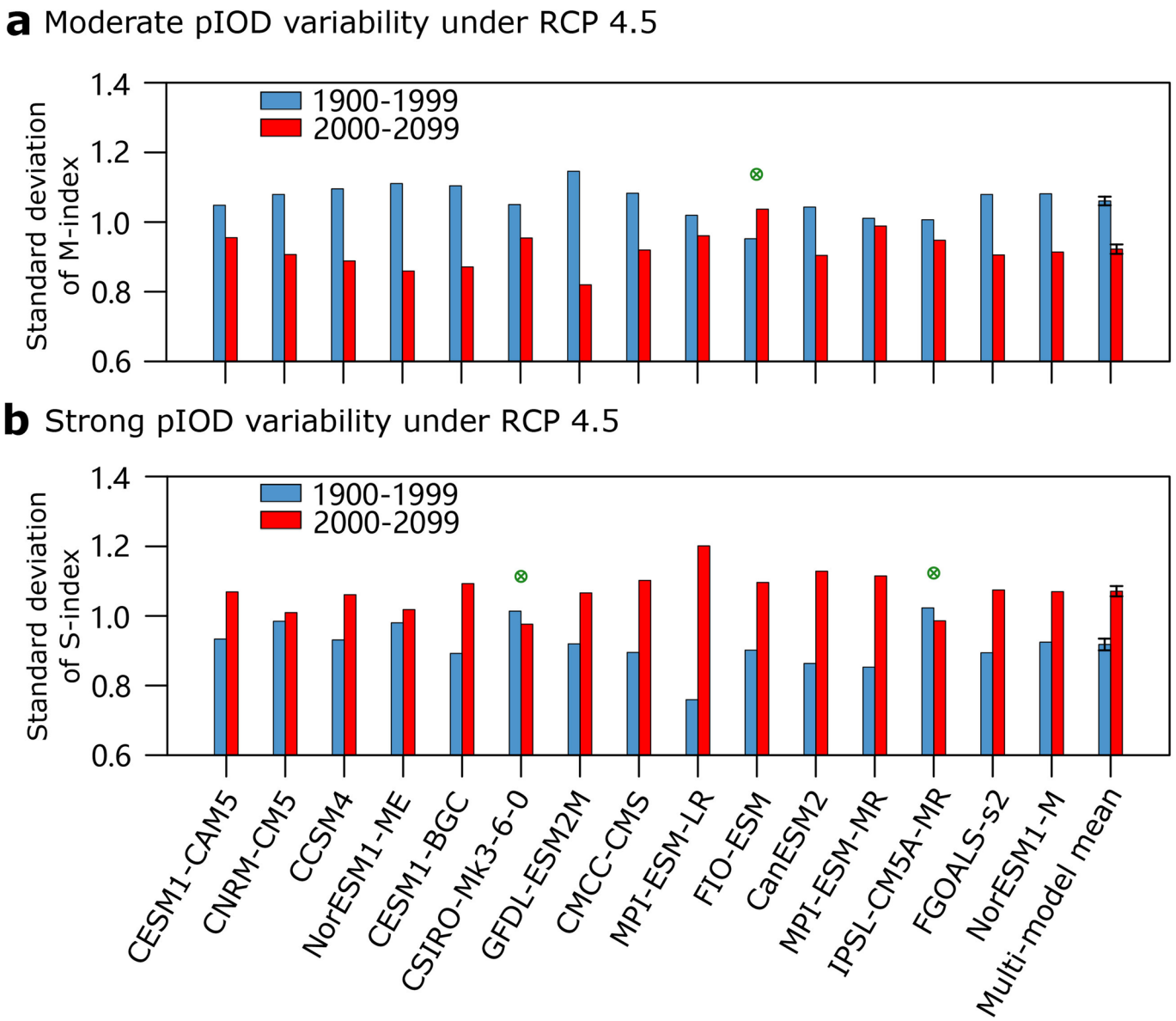

Extended Data Fig. 8 | Sensitivity of projected changes in pIOD variability to emission scenario. Shown are results for emission scenario RCP 4.5. **a**, **b**, Comparison of variability of the moderate pIOD (M-index) and strong pIOD (S-index), respectively, in the present-day (1900–1999) and future (2000–2099) climate in 15 out of 33 CMIP5 models that simulate a nonlinear coefficient α greater than 50% of the observed value. In **a**, a total of 14 out of the 15 models (93%) simulate a decrease in M-index variability in the future period (red bars) from that in the present-day period (blue bars). This leads to a multi-model mean decrease of 13%, statistically significant above the 95% confidence level, as indicated by the error bars. In **b**, a total of 13 out of the 15 selected models (87%) simulate an increase in S-index variability in the future climate, with a multi-model mean increase of 16%, statistically significant above the 95% confidence level. Models that simulate an opposite change to the multi-model mean are indicated by green circles. A total of 33 CMIP5 models are used here as outputs from CMCC-CESM and FGOALS-g2 are unavailable.

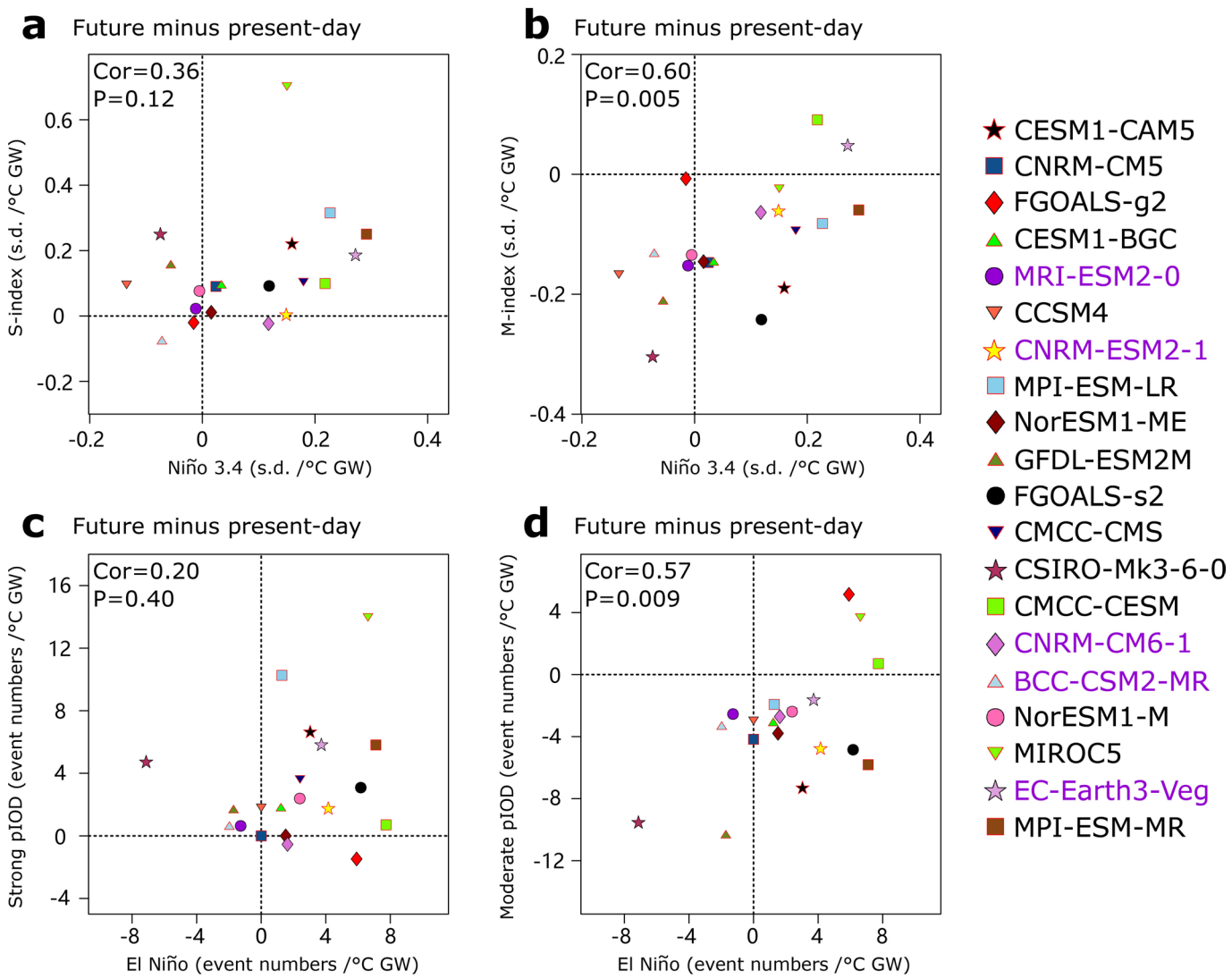

Extended Data Fig. 9 | Relationship between projected changes in ENSO and in pIOD. a, Scatter plot of changes in September, October, and November (SON) S-index variability versus changes in SON Niño3.4 index variability. The change is defined as the difference between the present-day (1900–1999) and future (2000–2099) period scaled by the corresponding increase in global mean SST in each model. **b**, Same as **a**, but between changes in SON M-index variability and in SON Niño3.4 index variability. **c, d**, Same as **a, b**, but for changes in strong pIOD (S-index>1.5 s.d.) or moderate pIOD (M-index>1.25 s.d.) frequency (events per 100 years) vs frequency of El Niño (Niño3.4>1.0 s.d.). The associated correlation coefficient and *P*-value are plotted. There is no relationship between changes in El Niño and S-index in **a** and **c**. Although there is a positive correlation in **b** and **d**, the changes in M-index and in El Niño are in the opposite direction, contravening the relationship between El Niño and M-index.

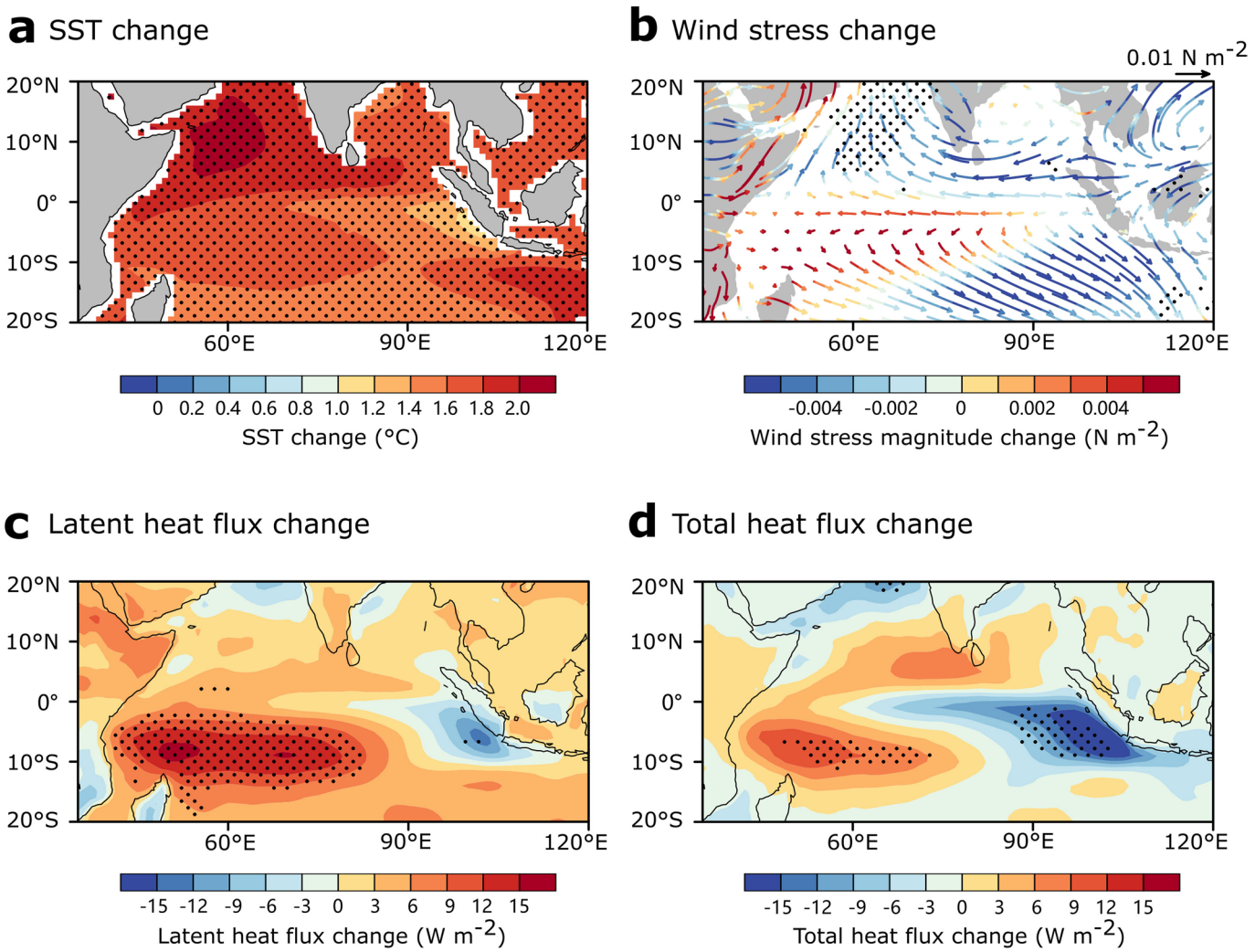

Extended Data Fig. 10 | Projected mean state change in the tropical Indian Ocean. Shown are averages over the 20 models that simulate a nonlinear coefficient α greater than 50% of the observed value. **a**, Multi-model ensemble averaged mean state changes of SON SST (in °C) between the future (2000–2099) and the present-day (1900–1999) climate. **b**, Same as **a**, but for the mean state change in surface wind stress (in N m^{-2}); changes in wind stress magnitude (in N m^{-2}) are indicated by colors. **c**, Same as **a**, but for the mean state change in latent heat flux (in W m^{-2}). **d**, Same as **a**, but for the mean state change in total heat flux (in W m^{-2}); positive values indicate an upward transfer of energy. Stippled areas indicate where changes are statistically significant above the 95% confidence level according to a two-tailed Student's *t*-tests.